HHS Public Access

Author manuscript

*J Magn Reson Imaging*. Author manuscript; available in PMC 2020 October 01.

Published in final edited form as:

*J Magn Reson Imaging*. 2020 October ; 52(4): 978–997. doi:10.1002/jmri.27105.

# Emerging MRI Techniques to Redefine Treatment Response in Patients With Glioblastoma

**Fabrício Guimarães Gonçalves, MD**[1,†], **Sanjeev Chawla, PhD**[2,†], **Suyash Mohan, MD, PDCC**[2,*]

[1]Department of Radiology, Children's Hospital of Philadelphia, Philadelphia, Pennsylvania, USA

[2]Department of Radiology, Perelman School of Medicine at the University of Pennsylvania, Philadelphia, Pennsylvania, USA

## Abstract

Glioblastoma is the most common and most malignant primary brain tumor. Despite aggressive multimodal treatment, its prognosis remains poor. Even with continuous developments in MRI, which has provided us with newer insights into the diagnosis and understanding of tumor biology, response assessment in the posttherapy setting remains challenging. We believe that the integration of additional information from advanced neuroimaging techniques can further improve the diagnostic accuracy of conventional MRI. In this article, we review the utility of advanced neuroimaging techniques such as diffusion-weighted imaging, diffusion tensor imaging, perfusion-weighted imaging, proton magnetic resonance spectroscopy, and chemical exchange saturation transfer in characterizing and evaluating treatment response in patients with glioblastoma. We will also discuss the existing challenges and limitations of using these techniques in clinical settings and possible solutions to avoiding pitfalls in study design, data acquisition, and analysis for future studies.

PRIMARY CENTRAL NERVOUS SYSTEM (CNS) tumors originate from cells within the brain, spinal cord, and meninges. In adults, the most common primary brain tumor is glioblastoma (GBM), which arises from glial cells. GBM is the most malignant of all primary brain tumors,[1] and is classified into IDH-wild-type and IDH-mutant, depending on the presence or absence of mutation in the IDH1 gene, which encodes isocitrate dehydrogenase 1, an enzyme that plays essential roles in normal cell metabolism.[2] Despite aggressive multimodal treatment, its prognosis has remained unfavorable, with a median overall survival limited to 14–16 months.[3]

Continuous developments in magnetic resonance imaging (MRI) have provided new insights into the diagnosis, classification, and understanding of tumor biology. Despite the optimization of sequences and protocols, the grading of gliomas based on conventional MRI frequently remains unreliable.[4] We believe that the integration of information from advanced neuroimaging techniques can further improve the diagnostic accuracy of conventional MRI.

*Address reprint to: S.M., 3400 Civic Center Blvd, Philadelphia, PA 19104, USA. suyash.mohan@pennmedicine.upenn.edu.
†Both authors have contributed equally to this work.

The purpose of this article is to overview the utility of advanced neuroimaging techniques such as diffusion-weighted imaging (DWI), diffusion tensor imaging (DTI), perfusion-weighted imaging (PWI), proton magnetic resonance spectroscopy ($^1$H MRS), and chemical exchange saturation transfer (CEST) in characterizing and evaluating treatment response in patients with GBM. We will also discuss the existing challenges and limitations of using these techniques in clinical settings and discuss possible solutions to avoid pitfalls in study design, data acquisition, and analysis for future studies.

## CLINICAL PRESENTATION

The clinical presentation of patients with GBM is variable, depending on tumor size and location. The duration of symptoms may be abrupt, mimicking a stroke, or prolonged, spanning over several years.[5] The main clinical symptoms are related to focal neurological deficits, increased intracranial pressure, and “seizures,” which remains the most common presenting symptom. Depending on location, focal neurological deficits, such as hearing loss, visual impairment, personality changes, hemiparesis, hemineglect, and aphasia, can occur, which are likely secondary to brain invasion and necrosis.[5] Headaches secondary to increased intracranial pressure can be present in up to 50% of patients.[6] Tumor-related headaches are usually unilateral with variable duration, may awaken patients from sleep, and be accompanied by focal neurological deficits, cognitive or behavioral symptoms, nausea, vomiting, and papilledema.[5] Seizures are the presenting symptoms in about 20–40% of patients, which could be simple partial, complex partial, or generalized. Seizures may also occur later in the disease course in as many as 50% of patients.[5,7] Patients are frequently diagnosed as part of an emergency department evaluation for one of the acute presentations above. During this visit, patients usually undergo first a computed tomography (CT) examination. Once confounding entities are excluded, and a mass lesion is detected, patients subsequently undergo an MRI examination.

## CONVENTIONAL IMAGING IN INITIAL ASSESSMENT OF GLIOBLASTOMA: ROLE AND LIMITATIONS

Neuroimaging plays an integral role in the initial diagnosis, prognosis, as well as in the assessment of treatment response in neuro-oncology. Commonly employed conventional anatomical MRI sequences include $T_1$-weighted imaging ($T_1$WI), $T_2$WI, fluid attenuation inversion recovery (FLAIR), $T_2$*WI gradient echo, and contrast-enhanced $T_1$WI images. These sequences provide refined anatomic detail, and the injection of a gadolinium-based contrast agent allows for the detection of the blood-brain barrier (BBB) compromise and leakage.

GBMs demonstrate a variable signal on $T_1$WI and T2WI, heterogeneous contrast enhancement, irregular margins, necrosis, hemorrhage, marked vasogenic edema, invasion into normal-appearing brain tissue, and corpus callosum infiltration.[8] The association of an irregular enhancing lesion with areas of hypo- or nonenhancing tumor infiltration and cortical expansion is particularly suggestive of high-grade infiltrating gliomas such as a GBM. Satellite lesions and intratumoral hemorrhage are also frequently encountered.[8]

Conventional MRI features are limited in reliably distinguishing various glioma grades and underlying pathophysiological mechanisms. Moreover, conventional MRI is limited in the differentiation of residual or recurrent tumor from treatment-related changes (Fig. 1). Furthermore, in some instances, GBM can be challenging to distinguish from other intracranial mass lesions such as solitary metastasis, lymphoma, atypical infections, and tumefactive demyelination. These limitations are significant to note, as they impact diagnosis, prognosis, as well as management approaches.[8]

The current standard of care treatment for GBM includes maximal safe resection followed by concurrent radiotherapy along with adjuvant temozolomide (CCRT).[9] Contrast-enhanced MRI (unless contraindicated) is the method of choice to estimate the extent of resection and to assess for any complications during surgery.[10] The first contrast-enhanced MRI should ideally be performed within 2 days after surgery in order to assess the extent of resection, but no later than 72 hours after surgery.[11] When baseline imaging is acquired beyond 72 hours, subacute hemorrhage/ischemia or reactive postsurgical enhancement may be confused with residual neoplasm. Postoperative blood in the surgical cavity may be a confounding factor due to its intrinsic T1 shortening effect, which may be difficult to distinguish from an enhancing lesion. Therefore, a direct comparison of pre- and postcontrast images, preferably obtained in the same imaging plane, is recommended. On baseline postoperative imaging, thin curvilinear enhancement may be seen along the margins of the resection cavity, which may represent postoperative changes, granulation tissue, micro-ischemia, and/or inflammation. Nevertheless, larger enhancing areas with nodular and mass-like configuration, similar in morphology to preoperative imaging, indicates residual neoplasm.[12]

## RESPONSE ASSESSMENT

Levin et al.[13] proposed the earliest response assessment criteria for malignant brain tumors in 1977, which was based on neurological examination, radionuclide scintiscan, and CT. In 1985, Zeltzer et al.[14] proposed criteria and definitions for response and relapse in different brain tumors in children, also based on CT. Subsequently, Macdonald et al.[15] suggested a new response assessment criteria for brain tumors in 1990, found initially on CT, and later extrapolated to MRI, in association with clinical assessment and corticosteroid use. The “Macdonald criteria” had many relevant limitations, including measuring tumors with irregular borders, interobserver variability, underestimation of tumoral components that lacked enhancement, lack of specific guidance for the evaluation of multifocal tumors, and the difficulty in measuring enhancing lesions in the wall of cystic or surgical cavities.

Although contrast enhancement is generally a reliable surrogate of brain tumor burden, some caveats and exceptions have been discovered as a result of different treatment mechanisms that affect vascular permeability. For example, increased vascular permeability from cytotoxic therapies, including radiotherapy and antineoplastic treatments, have been shown to result in increased contrast enhancement in the context of therapeutic benefit, a phenomenon called “pseudoprogression” (PsP).[16]

Additionally, clinical studies examining the efficacy of new antiangiogenic agents have noticed a substantial decrease in contrast enhancement, resulting in high response rates in

patients with bevacizumab and cediranib compared with other chemotherapies. It was assumed that this high response rate was due to the use of contrast enhancement as the primary tool for evaluation in the "Macdonald criteria," which resulted in a phenomenon called "pseudoresponse" (PsR), where contrast enhancement is falsely reduced due to changes in vascular permeability independent of an antineoplastic effect. Therefore, posttherapy effects such as PsP and PsR hinder a reliable assessment of treatment evaluation.[17]

To overcome the limitations of the "Macdonald criteria," the Response Assessment in Neuro-Oncology (RANO) criteria were developed in 2010.[18] According to the RANO criteria, which incorporates MRI and clinical factors, treatment response may be divided into complete response, partial response, stable disease, and progressive disease. Neuroimaging response should be determined in comparison to the tumor measurement obtained at pretreatment baseline for determination of response, and the smallest tumor measurement at either pretreatment baseline or after initiation of therapy should be used for determination of progression.

Albeit "RANO criteria" addresses several inconsistencies in the "Macdonald criteria," there are still several limitations to the current standard "RANO criteria" based on recent data. The bidirectional measurements of contrast-enhancing tumor size in RANO may overestimate tumor volume and result in higher reader discordance. The thresholds adopted to define response and true progression (TP) can be considered relatively arbitrary and not optimized. There could be a bias toward small tumors when thresholds based on "percentage change" are used. Nonenhancing progression is controversial due to the subjective nature of the interpretation. Studies have shown that evaluation of nonenhancing TP using $T_2$WI or FLAIR may be more complicated than usually understood, thus warranting further investigation before it can be integrated appropriately as an early radiographic endpoint. Finally, the introduction of new immunotherapeutic agents results in profound inflammation, leading to substantial changes in $T_2$ signal intensities as well as in areas of contrast enhancement.

In addition, RANO criteria based on conventional MRI are often equivocal in distinguishing between PsP, PsR, and TP, and present a considerable diagnostic challenge to distinguish these three clinical conditions. Hence, there is a critical demand to develop advanced neuroimaging biomarkers to access treatment response reliably.[19]

Recently, an update to the RANO criteria was proposed. These new criteria include the calculation of volumetric response, utilization of contrast-enhanced $T_1$ subtraction maps to increase enhancing lesion conspicuity, elimination of qualitative nonenhancing tumor assessment requirements, utilization of the postradiation timepoint as the baseline for newly diagnosed GBM response assessment, and the estimation of "treatment-agnostic" response assessment schemes for identifying PsP, PsR, and a confirmed durable response in newly diagnosed and recurrent GBM trials.[19]

There has been growing evidence that advanced MRI techniques such as DWI, PWI, $^1$H MRS, and CEST hold great potential in the accurate assessment of response. However, these

techniques have not yet been included in the most recent response assessment criteria. Therefore, further studies are necessary to validate the role of these techniques for response assessment in these patients.[18]

## DIFFUSION-WEIGHTED IMAGING

The biophysical mechanism of DWI is based on the microscopic random translational motion of water molecules in biological tissues. Water molecule diffusion follows the principles of Brownian motion. The magnitude of this motion is characterized by its apparent diffusion coefficient (ADC) values expressed in units of $mm^2/s$.[20] ADC depends on the nature of cellular packing, and the presence of intracellular organelles, cell membranes, and macromolecules in various tissue compartments. Variation in ADC values also reflects the alteration and redistribution of water molecules between intracellular and extracellular compartments of a tissue.

In gliomas, it has been reported that there exists an inverse correlation between ADC values and tumor grade.[21] High-grade tumors with tightly-packed tumor cells and reduced extracellular space demonstrate low ADC values.[22] Hence, it is expected that successful CCRT, leading to necrosis or cellular lysis, would reduce tumor cellularity and therefore lead to increased ADC values. On DWI, changes in the diffusivity pattern of a tumor might be used to monitor tumor response to a therapeutic intervention.

DWI is paramount to distinguish enhancing perioperative subacute ischemia from enhancing residual tumor on follow-up imaging by comparing areas of enhancement with DWI obtained at 24–48 hours of a postoperative MRI scan.[23] DWI can also help detect early tumor recurrence, especially in nonenhancing regions, with intact BBB. Logistic regression analysis has been used to demonstrate that areas of future GBM recurrence demonstrate a subtle, but significant, decrease in signal intensity on ADC maps and FLAIR images months before abnormal enhancement was evident.[24]

Since a reduction in the number of neoplastic cells following treatment precedes significant tumor size change, ADC may serve as an early imaging biomarker to predict treatment outcomes, monitor early treatment response, and detect recurrence.[20] In a subset of GBM patients, the development of a new focus of restricted diffusion during treatment may precede the development of a new enhancing tumor.[25] Persistently low ADC measurements similar to those observed in acute infarct can be seen in a subset of patients with antiangiogenic therapy, from coagulative necrosis, and are associated with improved clinical outcomes.[26]

Diffusion weighting is expressed as a b value, which is dependent on the characteristics of the diffusion sequence used. The b value increases with increasing diffusion weighting, and sufficient diffusion weighting is usually achieved with a b value of 1000 $s/mm^2$. The advent of stronger and faster gradients on the MR scanners has allowed us to use higher b values $\geq$3000 $s/mm^2$ and the ability to obtain images with a much greater degree of diffusion weighting. The appearance of the brain on high b-value diffusion images is significantly different from low b-value images, with white matter becoming relatively hyperintense and

the cortical gray matter becoming so hypointense that anatomical surface landmarks of the brain may be lost. The signal-to-noise ratio (SNR) also becomes an essential issue at higher b-value DW imaging due to the exponential loss in signal with increasing b values. Some studies[27] have also shown the potential of using a high b value DWI in the differentiation between PsR and true response after antiangiogenic treatment.

## DIFFUSION TENSOR IMAGING

A better method to model diffusion in a complex tissue is to use the diffusion tensor, a mathematical model of diffusion in 3D space. In DTI, a tensor model of diffusion consists of a 3 × 3 matrix derived from diffusivity measurements in at least six noncollinear/nonplanar directions. However, the use of more than six diffusion-encoding directions improves the accuracy of the tensor measurement for any arbitrary orientation. The diffusion tensor can be represented by a diffusion ellipsoid whose main axis is parallel to the principal diffusion direction within a voxel. The major and minor axes of the diffusion ellipsoid are defined by three orthogonal unit vectors known as eigenvectors. The length of each eigenvector is multiplied by a factor called the eigenvalue. Three eigenvalues, $\lambda_1$, $\lambda_2$, and $\lambda_3$ and three eigenvectors $v_1$, $v_2$, and $v_3$ define the shape and orientation of the ellipsoid, respectively. In the brain, water molecules are unable to diffuse freely due to natural barriers such as intracellular organelles and membranes, and white matter fibers and tracts (anisotropic diffusion). Hence, DTI benefits from this anisotropic water motion to estimate the axonal direction in vivo. DTI has been used to characterize normal tissue properties, in both diagnosis and prognosis of brain tumors in addition to guiding neurosurgical procedures.[28]

A comprehensive data modeling of DTI provides several scalar parameters such as mean diffusivity (MD), fractional anisotropy (FA), coefficient of linear (CL), planar (CP), and spherical (CS) anisotropies describing the shape of a diffusion ellipsoid. The most commonly used DTI indices in neuro-oncology are MD and FA. MD is comparable and mathematically equivalent to the ADC values and also provides similar physiological information.[29] FA is an index for the amount of diffusion asymmetry within a voxel whose value changes from 0 (isotropic) to 1 (maximally anisotropic). Higher values of FA correlate with greater directionality of the white matter tracts.[30] The geometric indices (CL, CP, and CS) have been used to differentiate GBM from metastasis and lymphoma,[31] TP from PsP,[32] brain infections from necrotic neoplasms,[33] and to evaluate treatment response to immunotherapy in GBM patients,[34] suggesting that directional organization of tissue microstructure may provide additional useful information.[35]

DTI can be used to detect tumoral infiltration of the adjacent normal-appearing white matter. Recently, our group[36] demonstrated that FA values from the corpus callosum could quantify occult tumor infiltration in GBM patients. Representative anatomical and DTI images from GBMs with and without corpus callosum involvement are shown in Fig. 2. Moreover, we reported[36] that FA may serve as a sensitive prognostic marker for prediction of overall survival in GBM patients, as patients with short survival and corpus callosum invasion had the lowest FA values from the corpus callosum regions compared to the other groups in our study (Fig. 3).

## PERFUSION-WEIGHTED IMAGING

PWI provides multiple additional parameters to overcome the intrinsic limitations of conventional MRI. PWI can demonstrate neovascularization, which translates into TP. Tumor neovascularization is known to show an extensive network of weak and poorly organized tumor vessels. Newly formed vessels are often large, tortuous, irregular, leaky, slow-flowing and uneven in diameter.[37] Leaky tumor vessels are depicted as an enhancement on conventional postcontrast $T_1$-weighted MRI. Nevertheless, with PWI, one can determine the blood volume and flow as well as the component of leakage, thus obtaining further information on the tumor vasculature.[17] The most commonly used PWI techniques are dynamic susceptibility contrast imaging (DSC), dynamic contrast-enhanced imaging (DCE), and arterial spin labeling (ASL).

### Dynamic Susceptibility Contrast

DSC is the most commonly employed PWI method in clinical neuro-oncology.[38] DSC involves the administration of a bolus of gadolinium-based contrast agent intravenously, followed by a series of rapidly acquired gradient or spin-echo images over the organ of interest. DSC utilizes the $T_2$* effect of the paramagnetic contrast agent that causes a transient decrease in signal intensity during the initial pass through the vasculature by creating a local magnetic field distortion around the vessels. By measuring the signal intensity as a function of time and fitting it to a mathematical model, various perfusion parameters such as blood volume, blood flow, and mean transit time can be extracted.[39] According to the American Society of Functional Neuroradiology (ASFNR) recommendations, DSC should be performed on a 1.5 or 3T MR system using $T_2$*-weighted gradient-echo sequences for higher SNR and sensitivity, with as short a relaxation time (TR) as possible, with echo time (TE) of 40–45 msec at 1.5T and 25–35 msec at 3T, and flip angles of 60–70°. Temporal coverage should be 90–120 total timepoints, with a total acquisition time of 2–3 minutes. Image acquisition should begin at least 30–50 time points before contrast injection via a power injector. A preload administration of a single contrast agent bolus, of one-fourth to single-dose (0.025-to 0.1-mmol/kg gadolinium) as a preload is given 5–10 minutes before the acquisition of dynamic imaging. The preload dose reduces the confounding $T_1$ effects from contrast agent leakage, mainly when high flip angle sequences are employed. A summary of the recommended acquisition parameters for DSC perfusion imaging can be found elsewhere.[40]

Multiple qualitative and semiquantitative indices can be derived from DSC data, namely: 1) cerebral blood volume (CBV), which is the volume of blood in a given region of brain tissue (measured in mL per 100 g of brain tissue); 2) cerebral blood flow (CBF), the volume of blood passing through a given region of brain tissue per unit time (measured in mL per minute per 100 g of brain tissue); 3) mean transit time (MTT), the average time (measured in seconds) it takes for blood to pass through a given region of brain tissue; 4) time-to-peak (TTP), defined as the time from initial contrast injection to peak (maximal) signal loss within the organ of interest; 5) bolus arrival time (BAT), defined as the interval between intravenous contrast injection and its first detection in tissue or a large feeding artery; 6) negative enhancement integral (NEI) is the total area under the signal intensity-time curve

during the first pass of contrast agent, also known as the area under the curve (AUC). This parameter reflects the total amount of contrast transiting through the regional vascular system and is roughly proportional to blood volume. The percentage signal recovery (PSR), the percentage of MR signal-intensity recovery relative to the precontrast baseline at the end of the first pass.[40]

To obtain CBV, the signal intensity-time curve is converted into a gadolinium concentration-time curve, and the conversion between signal intensity and gadolinium concentration is essentially a logarithmic transformation. The gadolinium concentration is assumed to be linearly proportional to the observed change in the $T_2$*-relaxation rate. CBV measurements are nonquantitative and can vary within the same tissue type, or the same patient, across different scan dates and different MRI scanners. As a result, CBV measurements are typically normalized to contralateral white matter tissue to obtain relative CBV (rCBV). As the size of the region of interest (ROI) and location must be carefully chosen, often by an experienced radiologist, this method often introduces unnecessary bias into the results and can be time-consuming.[41]

The DSC imaging acquisition with subsequent automatic rCBV, rCBF, and MTT color maps availability is a relatively fast process. Absolute DSC perfusion quantification is a more laborious process since it requires ROI manual segmentation. DSC is a technique that assumes that the contrast material remains in the intravascular compartment, which is not always the case, especially when dealing with leaky and tortuous capillaries of tumors. rCBV, however, may be underestimated or overestimated due to disruption in the BBB.[42] These unwanted leakage effects can be avoided by the preloading dose of contrast injection and by the use of leakage correction algorithms such as gamma variate functions.[42]

### Dynamic Contrast-Enhanced

DCE perfusion involves the acquisition of $T_1$-weighted images, generally using 3D-spoiled gradient recalled echo (SPGR) or fast low angle shot (FLASH) sequences before, during, and after the injection of gadolinium-based contrast agent. DCE measures $T_1$ changes in tissues over time after bolus administration of gadolinium. DCE is often performed for generating tissue perfusion parameters based on pharmacokinetic modeling that typically requires an additional precontrast $T_1$ mapping protocol. Full quantitative analysis of the DCE data requires conversion of signal intensity to the gadolinium concentration curve, selection of an appropriate tissue model, and estimation of model parameters from the fitted data.[43] In clinical settings, a model proposed by the Tofts-Kermode model is the most commonly used pharmacokinetic model to process the DCE data.[44] The most commonly used DCE-MRI-derived parameter is the volume transfer constant ($K^{trans}$) that determines the flux of gadolinium contrast agent from blood plasma to the extravascular extracellular space. Physiologically, $K^{trans}$ reflects tumor perfusion and vascular permeability. The other clinically relevant parameters include volume fraction of extravascular extracellular space in tissue ($v_e$) that might be related to ADC values and cellularity, and volume fraction of plasma space ($v_p$).[39,45] If DCE and DSC are acquired during the same examination, it is recommended that DCE is acquired prior to DSC, so that the first contrast injection for the DCE allows the estimation of vascular leakage using DCE and also works as the preload for

DSC.[39] The main limitations of DCE include the lower temporal resolution as compared with DSC and the lack of consensus for the optimal pharmacokinetic model. Since parameters acquired by different models are not comparable, those differences across different institutions may hinder the comparison of findings.[17]

### Arterial Spin Labeling

Arterial spin labeling (ASL) is an entirely noninvasive and contrast injection-independent PWI technique utilizing water molecules flowing inside arterial vessels as a contrast material in ASL. During imaging acquisition, these molecules are tagged magnetically prior to entering the region to be studied and then followed until they reach the area of interest.[46] CBF values can be calculated by the differences in signal between the labeled images and the nonlabeled control images.[46,47] Among the multiple ASL methods available, pseudocontinuous ASL is now widely accepted as the method of choice. During a pseudocontinuous acquisition, blood is labeled from 2–4 seconds. After a delay of 1.5–2 seconds, which allows the labeled blood to arrive in the brain tissue, images are acquired.[47] One major advantage of ASL is the lack of leakage effects. Leakage correction is, therefore, unnecessary in ASL.[49] ASL scanning times are longer than DSC and DCE, due to lower SNR, which may increase the risk of motion artifacts.[39] In comparison with the other PWI methods, ASL offers fewer parameters, with CBF being the most frequently used parameter in routine clinical practice. Nevertheless, it has been demonstrated that CBF obtained by ASL correlates well with rCBV derived from DSC acquisition.[47]

### PWI Predicting and Evaluating Treatment Response

Some studies have suggested that pretreatment $rCBV_{max}$ can be used as a prognostic marker for overall survival in patients with GBM. In particular, patients with high pretreatment $rCBV_{max}$ demonstrated lower survival in comparison with patients with low pretreatment $rCBV_{max}$.[50] We believe that these results could have a potential clinical benefit and, in the future, may aid in individualized treatment planning because patients with high pretreatment $rCBV_{max}$ can be offered upfront alternative treatment strategies, including bevacizumab, immunotherapy, or other therapies targeted toward increased survival.

Treatment response assessment is more reliably performed with PWI than conventional MRI. A recent meta-analysis has shown a pooled sensitivity and specificity of anatomical MRI of 68% (95% confidence interval [CI] 51–81) and 77%,[45–93] respectively, whereas the pooled sensitivity and specificity of DSC were of 87%[82–91] and 86%[77–91] and the pooled sensitivity and specificity of DCE were of 92%[73–98] and 85%,[76–92] respectively.[51–53] Several studies[51] have demonstrated that rCBV values are higher in TP than in treatment-related effects. rCBV values are higher in tumors, indicating their hyperperfusion volume. However, there is a wide variability of the optimum rCBV threshold for differentiating between TP and treatment-related effects, ranging from 0.71–3.7.[51] Further attempts should be aimed at validating cutoff values and to standardize perfusion measurements, allowing the identification of the best cutoff for clinical implementation.[17]

rCBF has also been used for differentiating tumor recurrence from stable disease with a diagnostic accuracy comparable to that of rCBV.[54] Additionally, semiquantitative DSC

parameters such as peak height and percentage of signal recovery have been found to be significantly higher in TP than PsP.[55] Moreover, these heuristic parameters are highly affected by the gain factor of the acquisition systems, contrast agent volume, and injection rate. As a result, these factors can easily change the shape of the signal-intensity time curves, precluding accurate estimation of the true concentration of contrast agent in the tissues, and thus making comparison and quantification difficult. Moreover, these descriptive parameters provide no physiologic information about the lesion of interest.

DCE demonstrates a superior diagnostic accuracy to differentiate TP from PsP.[51] This higher accuracy can be explained by the $K^{trans}$ parameter, which reflects the higher capillary permeability of leaky tumor vessels. In DCE, most experience has been built up with AUC along with $K^{trans}$. The $K^{trans}$, $v_e$, and AUC values in the normal white matter were significantly different from those in the radiation necrosis and recurrent gliomas. The only significantly different hemodynamic parameters between recurrent tumor and radiation necrosis were $K^{trans}$ and AUC, which were significantly higher in the recurrent glioma group than in the radiation necrosis group ($P \leq .0184$). A $K^{trans}$ cutoff value higher than 0.19 $min^{-1}$ showed 100% sensitivity and 83% specificity for detecting recurrent gliomas, whereas an AUC cutoff value higher than 15.35 had 71% sensitivity and 71% specificity.[56]

There is a significant difference in $K^{trans}$ values between patients with TP and PsP, with higher values for the former.[57] A difference in mean $v_e$ values demonstrated a prognostic accuracy of 88% when a cutoff value of 0.873 was used.[57] However, the paucity of uniform thresholds due to a lack of uniformity in data acquisition and pharmacokinetic models remains troublesome.

Studies evaluating ASL to assess treatment response in GBM are scarce. Three ASL studies[54] (DOI:10.1007/s00330-017-4789-9) (DOI:10.1177/0284185112474916) reported unsatisfactory diagnostic accuracy, with broad differences in sensitivity and specificity. On ASL, TP is seen as areas with high rCBF values. ASL has shown higher imaging quality in comparison to DSC to differentiate TP and PsP using rCBF values.[58] In another study,[58] ASL and DSC had similar results in differentiating TP and PsP; however, DSC reached a higher diagnostic accuracy. In contrast, another investigator suggested that ASL could outperform DSC when using a normalized CBF cutoff ratio of 1.3.[59]

## PROTON MAGNETIC RESONANCE SPECTROSCOPY

Several studies,[60–64] including from our group, have reported the utility of $^1$H MRS for studying brain tumor metabolism with promising results in the evaluation of neoplasm grade, discrimination between types of neoplasms, differentiation of recurrent tumors from radiation injury, and determination of prognosis and response to treatment. In the clinical setting, $^1$H MRS is generally performed either as a single voxel technique (SVS) or as a slab comprised of several voxels (multivoxel spectroscopy / chemical shift imaging [CSI]). However, SVS or CSI $^1$H MRS may suffer from an incomplete sampling of the neoplasm. Moreover, the sampled voxels might include the external margins of the necrotic areas or peritumoral regions, or both. Thus, metabolite levels in such lesions might be influenced by the contribution from different tissue compartments of a neoplasm.

On the other hand, relatively new $^{1}$H MRS sequences such as the 3D-echo planar spectroscopic imaging (3D-EPSI) allow acquisition of metabolite maps with an excellent spatial resolution that can be spatially coregistered to anatomical images to facilitate mapping of metabolite alterations from different regions of a neoplasm with less probability of partial volume averaging. A representative postcontrast $T_1$-weighted image and corresponding Cho/NAA map from a patient with GBM are shown in Fig. 4. The potential of 3D-EPSI in characterizing glioma grades,[65] mapping glycine distribution in gliomas,[65] planning radiation therapy,[66] identifying residual tumor following radiation therapy,[67] evaluating response to epigenetic modifying agents in recurrent GBM,[68] evaluating treatment response to tumor treating fields,[63] differentiating TP from PsP,[62] and in assessing the effect of whole-brain radiation therapy on normal brain parenchyma in patients with metastases has been reported.[69]

In neuro-oncology, major metabolites that are typically observed on $^{1}$H MRS spectrum are N-acetylaspartate (NAA), choline (Cho), lactate (Lac), mobile lipids, creatine (Cr), glutamate (Glu), glutamine (Gln), glycine (Gly), myoinositol (ml), glutathione (GSH), and 2-hydroxyglutarate (2-HG). NAA shows the largest signal in a normal healthy brain and is considered a putative marker of neuronal density and viability and generally decreases in gliomas.[70] The Cho signal is a composite of free choline, phosphocholine (PC), and glycerophosphocholine (GPC), which are the precursors and breakdown products of the main membrane phospholipid phosphatidylcholine. The intensity of this resonance is associated with cell proliferation and cell signaling and is usually elevated in brain neoplasms, including GBM.[71] However, the lack of Cho elevation can be seen in some lower-grade brain neoplasms.[72] Therefore, it has been recommended that low Cho levels should not prevent us from considering the possibility of a primary brain neoplasm. Lac is the final byproduct of anaerobic glycolysis and enhanced in cancer as part of the Warburg effect.[73] Lipids (fatty acid, lipid droplets, or triglycerides) are rarely observed in the normal brain, but are often increased in glial tumors and are associated with cell death and increased necrosis.[7] The Cr signal is a composite of creatine and phosphocreatine (PCr), which are involved in energy metabolism via the creatine kinase reaction. Cr levels vary within normal brain regions and, in some cases, with tumorigenesis.[75] Glu is the most abundant amino acid in the brain and an essential neurotransmitter. In gliomas, glutaminolysis is often required for tumor growth as an anaplerotic source of carbon complementary to glucose metabolism.[76] Representative spectra from high and low rCBV regions of a neoplasm are shown in Fig. 5.

Several studies have reported that glioma patients whose lesions harbor IDH mutations are associated with better prognosis, regardless of histological grade, and these patients demonstrate more prolonged survival than those with IDH wildtype. Few studies[77] have used modified $^{1}$H MRS sequences in detecting resonances for 2HG. The oncometabolite, 2HG, has been proposed as a putative biomarker for IDH-specific genetic profile for gliomas. Recently,[78] we also reported our initial experience of identifying patients with IDH mutation using 2D correlation spectroscopy (COSY) with an ultrahigh-field (7T) MR system.

Several studies have also demonstrated the potential of $^{1}$H MRS in evaluating treatment response in GBM patients who underwent CCRT following surgery. Some studies[79] have demonstrated that increases in Cho/NAA and/or Cho/Cr ratios are significantly higher in patients with recurrent tumors than those with radiation necrosis. A meta-analysis of 455 GBM patients treated with radiotherapy concluded that $^{1}$H MRS alone has moderate diagnostic performance in differentiating glioma recurrence from radiation necrosis using Cho/Cr and Cho/NAA metabolite ratios, and strongly recommended its use only in combination with other advanced imaging technologies.[80] Since the pathogenesis of PsP and radiation necrosis is similar, it may be assumed that these two conditions would exhibit similar metabolite patterns. Indeed, the investigators of a previous study reported a lower Cho/NAA ratio and higher lipid levels in PsP than those patients with TP.[81] However, this study used single voxel or single slice multivoxel $^{1}$H MRS techniques and, therefore, was constrained by the limited overall spatial coverage of the neoplastic lesions. We believe that one of the reasons for the poor diagnostic performance of $^{1}$H MRS in differentiating tumor recurrence and radiation necrosis in the meta-analysis mentioned above may be because of contamination from different tissue compartments while using large voxel size $^{1}$H MRS methods.

On the other hand, alternate methods such as 3D-EPSI provide high-resolution metabolite maps from the entire brain that can help us in simultaneously probe metabolite profiles from different areas of a neoplasm.[69,82] Recently, we distinguished TP from PsP in GBM patients with a sensitivity of 94% and a specificity of 87% using 3D-EPSI.[62] Representative anatomical images, Cho/NAA maps, and corresponding reresection histology photomicrographs from a TP and a PsP patient are shown in Fig. 6. In additional studies from our group, we employed 3D-EPSI in assessing treatment response to anti-EGFRvlll chimeric antigen receptor T-cell therapy[34] and tumor treating fields[63] in patients with GBM. These studies indicate that 3D-EPSI may be a valuable tool to study brain tumor metabolism and assess for treatment response.

## CHEMICAL EXCHANGE SATURATION TRANSFER (CEST)

CEST is a relatively novel metabolic imaging technique that allows the detection of specific endogenous and exogenous molecules that are present at very low concentrations (μM to mM range). In CEST imaging, exchangeable solute protons, such as hydroxyls (-OH), amides (-NH), and amines (-NH2) that resonate at a frequency different from the bulk water protons (off-resonance frequencies for -OH, -NH and -NH2 protons are ~0.5–1.5 ppm, ~3.5 ppm, and 1.8–3.0 ppm, respectively) are selectively saturated using radiofrequency irradiation. This saturation is subsequently transferred to bulk water when solute protons exchange with water protons leading to a decrease in the water signal proportional to the concentration of solute molecules. While the saturation pulse is being applied, this process continues to decrease the water magnetization. Simultaneously, longitudinal relaxation processes return the saturated proton spins to their thermal equilibrium state until the system reaches a steady-state condition or the saturation pulse is turned off. The reduction in the water signal can be imaged with any fast imaging pulse sequences. The acquisition of CEST-weighted images must be rapid before $T_1$ relaxation reduces the amplitude of the CEST signal. For a similar reason, CEST imaging should be acquired before the administration of

gadolinium-based contrast agents. CEST contrast requires that a distinct chemical shift difference (Δω) between water and the exchangeable proton on the solute is preserved, and the exchange rate (ksw) needs to be in the slow to an intermediate regime in the nuclear magnetic resonance (NMR) time scale such that ksw ≤ Δω.

The frequency-dependent saturation effects are visualized similar to the magnetization transfer (MT) technique by plotting the water saturation (Ssat) normalized by the signal without saturation (S0) as a function of saturation frequency. This gives rise to a Z-spectrum or CEST spectrum that is characterized by the symmetric direct saturation (DS) around the water frequency, which leads to the assignment of 0 ppm to the water frequency. This DS effect may interfere with the detection of CEST signals, which is addressed by using the symmetry of the DS through MT ratio (MTR) asymmetry analysis:

$$\begin{aligned} \mathrm{MTRasym}(\Delta\omega) &= \mathrm{MTR}(\Delta\omega) - \mathrm{MTR}(-\Delta\omega) \\ &= \mathrm{Ssat}(-\Delta\omega)/\mathrm{S0} - \mathrm{Ssat}(\Delta\omega)/\mathrm{S0} \end{aligned}$$

Several factors such as the concentration of solutes, number of exchangeable protons, exchange rate, temperature, and pH of the local environment, $T_1$, $T_2$, saturation frequency, amplitude, duration of saturation frequency, and magnetic field strength regulate the CEST contrast on imaging.[83]

The CEST signal originates from the endogenous mobile proteins/peptides and metabolites such as Glu, lac, mI, and glucose that play crucial roles in tumor development, growth, and progression. Therefore, studying these macromolecules and metabolites may help us in understanding the brain tumor microenvironment and evaluating response to targeted therapies.

### Amide Proton Transfer (APT)

APT imaging is a CEST technique that measures a reduction in bulk water intensity due to the chemical exchange of labile amide protons present within the peptide bonds of endogenous mobile proteins and peptides in tissues. Amide protons resonant at about 8.3 ppm on the MR spectrum, and hence have a chemical shift 3.5 ppm downfield from water. Due to the very slow exchange rate (~30 $s^{-1}$) of amide protons, it is possible to obtain nearly complete saturation using a low-power, long-duration saturation pulse. Given the slow exchange rate of amide protons, APT imaging can also be performed even at 3T field strength. It has been reported that the APT signal is very sensitive to variations in pH levels, as lower pH in the ischemic regions leads to the diminished APT exchange rate, and consequently, a decline in the CEST effect is observed. Because of excellent sensitivity to pH, it is possible to use APT for determining the pH of tissues after proper calibration of the signals.

It is widely believed that active tumor cells express higher concentrations of mobile protein and peptide components.[85,86] Also, metabolically active tumors produce an excess of lactic acid in the extracellular tumor microenvironment. This decrease in tumor pH should generate lower APT contrast due to slower exchange rate of amide protons because the chemical exchange of protons from the amide group to water is base-catalyzed. Despite

these two counteracting mechanisms, higher APT contrast is generally observed from neoplastic regions compared to normal tissues. Some studies have shown the great potential of APT-weighted imaging in delineating malignant neoplastic infiltration from peritumoral vasogenic edema, in differentiating histopathological grades, and in discriminating high-grade gliomas from primary cerebral lymphomas.[87] APT imaging can also reliably distinguish recurrent tumor from radiation necrosis.[88] Additionally, the intensity of the APT signal was shown to decrease in irradiated tumors at 3 days and 6 days posttreatment periods relative to baseline, suggesting that APT may be useful in evaluating treatment response in brain tumors. The APT signal is also a valuable imaging biomarker for distinguishing TP from PsP in GBM patients. Some studies have documented significantly higher APT signals in TP cases than those with PsP.[85] In contrast to TP, there are fewer mobile cytosolic proteins and peptides in regions of brain injury associated with PsP, due to lower cellular density and disrupted cytoplasm. Collectively, these studies suggest that APT that is based on the CEST mechanism is fast emerging as a novel molecular MRI technique in neuro-oncology.

### Glutamate (GLU)-CEST

Glu is the most important excitatory neurotransmitter in the central nervous system and plays a vital role in tissue bioenergetics.[89] It has been demonstrated that Glu exhibits a pH and concentration-dependent CEST effect (Glu-CEST) between its amine group observed at ~3.0 ppm downfield from bulk water protons. Using $^{1}$H MRS, some previous studies have reported high Glx (Glu and Gln) in GBM relative to the normal brain parenchyma.[60] Elevated levels of Glx have also been observed on in vitro $^{1}$H MRS studies of perchloric acid extracts of GBM specimens.[90] In addition to its role as an energy fuel, Glx is involved in the cellular anabolic pathways. In particular, it is essential for the synthesis of purine and pyrimidine bases as a carbon (via aspartate) and nitrogen donor and, therefore, necessary for tumor cell growth.[91]

Moreover, tumors have been shown to release Glu at high levels, which may stimulate tumor cell proliferation via activation of Glu receptors. As GBM is known to infiltrate into the surrounding brain parenchyma, it has been observed that Glu is involved in facilitating tumor invasion by causing excitotoxic damage to the normal brain, thereby paving a pathway for tumor migration.[92] Moreover, the peritumoral region is considered the primary area responsible for epileptogenesis, and increased levels of Glu in the peritumoral region has been implicated in the pathobiology of glioma-associated seizure activities.[92,93]

Our group[94] developed a CEST method for imaging Glu (Glu-CEST) that can be utilized to generate high-resolution parametric maps to better understand the role of this crucial metabolite in studying brain tumor metabolism. In a recent study, increased peritumoral Glu-CEST contrast was associated with both recent seizures and drug-refractory epilepsy in patients with grade II–III gliomas, thereby substantiating the notion that peritumoral region is an epileptogenic zone.[95] In an ongoing project, we are currently investigating the potential of a 7T Glu-CEST sequence in detecting occult neoplastic infiltration into the normal brain by means of evaluating the extent of glutamatergic excitatory activity (unpublished data, Fig. 7). We believe that better visualization of neoplastic spread in normal-appearing brain

regions may help clinicians to plan surgery and/or radiation therapy in a more controlled and effective manner, thereby preserving eloquent brain functions.

## IMPORTANCE OF MULTIPARAMETRIC ANALYSIS

Multiparametric analysis is an evolving method in which multiple quantitative MRI techniques are analyzed in combination in order to overcome the intrinsic limitations of conventional MRI and to potentiate the individual value of each advanced MRI technique in isolation. Quantitative data obtained from metabolic and physiologic techniques such as DWI, DTI, DSC, DCE, ASL, or $^{1}$H MRS can be combined and analyzed with multivariate logistic regression, analysis of variance, or even with artificial intelligence (AI) tools to determine the optimal parameter/s and thresholds for addressing a specific question. Multiparametric MRI has been widely used to differentiate necrotic GBM from brain infections,[33] to differentiate GBM from solitary brain metastasis,[96] predict treatment response in GBM patients, to differentiate radiation necrosis from recurrent tumor,[97] to assess tumor invasiveness,[98] and in survival prediction.[99]

Representative anatomical images, MD, FA, CL, CP, and CBV maps, each from a patient with pyogenic abscess, and necrotic GBM, are shown in Figs. 8 and 9, respectively. The combination of DTI metrics and rCBV can help in the differentiation of necrotic GBM from brain metastasis and primary cerebral lymphoma. A multiparametric data analysis approach has also been widely used to evaluate treatment response in patients with GBM (Figs. 10 and 11). In the past, we used advanced MRI techniques in identifying TP or PsP with high sensitivity and specificity.[32] We also developed a classification model by incorporating FA, CL, and $rCBV_{max}$ in multivariate logistic regression analyses to discriminate TP from PsP with an accuracy of 90%.

While assessing the therapeutic effect of anti-EGFRvIII chimeric antigen receptor T-cell therapy in patients with recurrent GBM, our group recently[34] demonstrated that progression probability values derived from multiparametric MRI might allow a more accurate evaluation of treatment response than the use of individual parameters in isolation. Some other studies have also demonstrated the potential of multiparametric MRI in assessing treatment response to immunotherapies and targeted therapies in GBM patients.[100]

## EMERGING APPLICATIONS OF ARTIFICIAL INTELLIGENCE

Artificial intelligence (AI), machine learning (ML), neural networks (NNs), deep learning (DL), and convolution neural networks (CNNs) are major components of data science that have driven significant attention into the neuro-oncology domain lately (Fig. 12).

AI is an overarching term that encompasses any task executed by a computer that generally requires human intelligence.[101] ML is a component of data science focused on algorithms that enable computers to perform predictions about a new dataset using already trained data (Fig. 13). ML algorithms can be further classified as supervised and unsupervised.[102] Supervised ML algorithms are trained on a human-labeled dataset, which subsequently provide classification or regression on unlabeled data. The most common supervised ML techniques are linear and logistic regression, support vector machines (SVMs), naive Bayes,

decision trees, and random forest methods. In unsupervised ML, algorithms may identify undisclosed patterns for unlabeled datasets that are unrecognized in humans. The most common unsupervised machine learning methods include K-means, mean shift, affinity propagation, hierarchical clustering, Gaussian mixture modeling, and self-organizing maps.[102] Many AI techniques have been deployed to assist in glioma management. Several AI algorithms have already been employed to predict tumor grading, underlying genetic mutations, and survival rates; to automate diagnosis from histopathological slides; to segment tissues for surgical planning; and to monitor patients after treatment.[103]

Approaches with logistic regression classifiers,[104] SVM,[105,106] and NNs,[107] have suggested that AI algorithms may be used to predict tumor grade based on imaging features. Some studies[103] have also demonstrated that the prediction of tumor genomics from imaging data may be performed by AI algorithmic radiomics with a high accuracy rate. Radiomics is a broad term that comprises a set of computational methods that extract quantitative features from imaging that are beyond the human eye's ability to detect.[108,109] Previous studies have demonstrated ML-based algorithms predicting genetic mutations from imaging. The most frequently studied genetic mutations are the presence of IDH mutations,[103,110–113] $O^6$-methylguanine-DNA methyltransferase (MGMT) promoter methylation,[114–116] and the codeletion of chromosome arms 1p/19q, which are associated with better treatment response and survival rates.[117] In addition, ML algorithms have been used to extract data from genetic databases, thereby clustering GBM patients into different transcriptional subtypes to predict the prognosis and treatment response.[118]

Preoperative planning has also been assessed by AI algorithms such as CNNs, SVM, and random forest algorithms with at least moderate accuracy. AI algorithms have already been used for tumoral segmentation,[119–121] to differentiate voxels representing viable neoplasm vs. edema vs. normal brain tissue,[117,122–125] and for tumor localization.[126] AI has also been applied for intraoperative planning, aiding neurosurgeons to resect the maximum amount of tumor and the minimum amount of viable tissue. DL methods, coupled with hyperspectral imaging, were able to accurately (about 80%) differentiate neoplastic tissue from adjacent nontumoral brain tissues.[127]

The creation of slide scanners, which can digitalize microscopic slides into high-quality image files (computational histopathology), has made possible the inclusion of AI into the pathology realm.[128,129] SVM and decision trees have already been used to segment and classify cells on smear preparations of gliomas with high accuracy.[130] CNNs also have been used to extract significant histopathological features of a GBM from a slide with high accuracy.[131] SVM algorithms have been employed for diagnosis and glioma grading (grades II, III, and IV) on slide images with an accuracy of about 90%.[132]

Few studies are available involving the application of AI to differentiate treatment effects from tumor progression. An SVM classifier has been trained to diagnose PsP vs. TP in GBM patients treated with surgery and CCRT with high sensitivity and specificity of the classifier for PsP.[133] A CNN developed to differentiate TP vs. PsP in patients with GBM had an acceptable performance and a high AUC.[134] Several AI algorithms have been developed to predict the survival in glioma patients, with superior accuracy compared to conventional and

advanced MRI techniques.[134–138] AI also has the potential to impact the field of radiotherapy positively, assisting in patient selection, segmentation, simulation, treatment planning, quality assurance, and follow-up.[127]

In conclusion, GBM is the most common and most fatal of all primary malignant brain tumors in adults. Diagnosis and treatment response evaluation remain highly dependent on neuroimaging. Despite aggressive multimodal treatment, the prognosis has remained poor. Continuous developments in neuroimaging techniques have provided new insights into the understanding of the underlying tumor biology. Conventional MRI sequences provide refined anatomic detail and detection of BBB integrity and leakage. Multiparametric MRI combining advanced MRI techniques such as DWI, DTI, DSC, DCE, $^{1}$H MRS, Glu-CEST, and APT imaging are useful to accurately assess treatment response, particularly with the advent of novel targeted therapies. We believe that with continued advances in personalized medicine and better understanding and availability of these emerging neuroimaging techniques powered by AI tools, will improve the quality of life and overall outcome in these patients.

## REFERENCES


1. Lapointe S, Perry A, Butowski NA. Primary brain tumours in adults. Lancet 2018;392(10145):432–446. https://linkinghub.elsevier.com/retrieve/pii/S0140673618309905. [PubMed: 30060998]
2. Yan H, Parsons DW, Jin G, et al. IDH1 and IDH2 mutations in gliomas. N Engl J Med 2009;360(8):765–773. 10.1056/NEJMoa0808710. [PubMed: 19228619]
3. Thakkar JP, Dolecek TA, Horbinski C, et al. Epidemiologic and molecular prognostic review of glioblastoma. Cancer Epidemiol Biomarkers Prev 2014;23(10):1985–1996. 10.1158/1055-9965.EPI-14-0275. [PubMed: 25053711]
4. Law M, Yang S, Wang H, et al. Glioma grading: Sensitivity, specificity, and predictive values of perfusion MR imaging and proton MR spectroscopic imaging compared with conventional MR imaging. AJNR Am J Neuroradiol 2003;24(10):1989–1998. http://www.ajnr.org/content/24/10/1989.abstract. [PubMed: 14625221]
5. Omuro A, DeAngelis LM. Glioblastoma and other malignant gliomas: A clinical review. JAMA 2013 6;310(17):1842–1850. 10.1001/jama.2013.280319. [PubMed: 24193082]
6. Forsyth PA, Posner JB. Headaches in patients with brain tumors: A study of 111 patients. Neurology 1993;43:1678–1678. 10.1212/wnl.43.9.1678. [PubMed: 8414011]
7. Perry J, Zinman L, Chambers A, et al. The use of prophylactic anticonvulsants in patients with brain tumours-a systematic review. Curr Oncol 2006;13(6):222–229. https://www.ncbi.nlm.nih.gov/pubmed/22792022. [PubMed: 22792022]
8. Pope WB, Brandal G. Conventional and advanced magnetic resonance imaging in patients with high-grade glioma. Q J Nucl Med Mol Imaging 2018;62(3):239–253. 10.23736/S1824-4785.18.03086-8. [PubMed: 29696946]
9. Stupp R, Mason WP, van den Bent MJ, et al. Radiotherapy plus concomitant and adjuvant temozolomide for glioblastoma. N Engl J Med 2005;352(10):987–996. 10.1056/NEJMoa043330. [PubMed: 15758009]
10. Ekinci G, Akpinar IN, Baltacioglu F, et al. Early-postoperative magnetic resonance imaging in glial tumors: prediction of tumor regrowth and recurrence. Vol. Eur J Radiol 2003;45:99–107. 10.1016/s0720-048x(02)00027-x.
11. Zikou A, Sioka C, Alexiou GA, Fotopoulos A, Voulgaris S. Argyropoulou MI. Radiation necrosis, Pseudoprogression, pseudoresponse, and tumor recurrence: Imaging challenges for the evaluation of treated gliomas. Contrast Media Mol Imaging 2018; 2018:6828396. 10.1155/2018/6828396.

12. Oser AB, Moran CJ, Kaufman BA, Park TS. Intracranial tumor in children: MR imaging findings within 24 hours of craniotomy. Radiology. 1997;205(3):807–812. 10.1148/radiology.205.3.9393539. [PubMed: 9393539]
13. Levin VA, Crafts DC, Norman DM, Hoffer PB, Spire JP, Wilson CB. Criteria for evaluating patients undergoing chemotherapy for malignant brain tumors. J Neurosurg 1977;47(3):329–335. 10.3171/jns.1977.47.3.0329. [PubMed: 894339]
14. Zeltzer PM, Friedman HS, Norris DG, Ragab AH. Criteria and definitions for response and relapse in children with brain tumors. Cancer 1985;56(7):1824–1826. 10.1002/1097-0142(19851001)56:7+<1824::aid-cncr2820561321>3.0.co;2-h. [PubMed: 3896461]
15. Macdonald DR, Cascino TL, Schold SC Jr, Cairncross JG. Response criteria for phase II studies of supratentorial malignant glioma. J Clin Oncol 1990;8(7):1277–1280. 10.1200/JC0.1990.87.1277. [PubMed: 2358840]
16. Brandsma D, Stalpers L, Taal W, Sminia P, van den Bent MJ. Clinical features, mechanisms, and management of pseudoprogression in malignant gliomas. Lancet Oncol 2008;9:453–461. 10.1016/s1470-2045(08)70125-6. [PubMed: 18452856]
17. van Dijken BRJ, van Laar PJ, Smits M, Dankbaar JW, Enting RH, van der Hoorn A. Perfusion MRI in treatment evaluation of glioblastomas: Clinical relevance of current and future techniques. J Magn Reson Imaging 2019;49(1):11–22. 10.1002/jmri.26306. [PubMed: 30561164]
18. Wen PY, Macdonald DR, Reardon DA, et al. Updated response assessment criteria for high-grade gliomas: Response assessment in neuro-oncology working group. J Clin Oncol 2010;28:1963–1972. 10.1200/jco.2009.26.3541. [PubMed: 20231676]
19. Ellingson BM, Wen PY, Cloughesy TF. Modified criteria for radiographic response assessment in glioblastoma clinical trials. Neurotherapeutics. 2017;14(2):307–320. 10.1007/s13311-016-0507-6. [PubMed: 28108885]
20. Kim M, Kim HS. Emerging techniques in brain tumor imaging: What radiologists need to know. Korean J Radiol 2016;17(5):598–619. 10.3348/kjr.2016.17.5.598. [PubMed: 27587949]
21. Sugahara T, Korogi Y, Kochi M, et al. Usefulness of diffusion-weighted MRI with echo-planar technique in the evaluation of cellularity in gliomas. J Magn Reson Imaging 1999;9(1):53–60. https://www.ncbi.nlm.nih.gov/pubmed/10030650. [PubMed: 10030650]
22. Ellingson BM, Malkin MG, Rand SD, et al. Validation of functional diffusion maps (fDMs) as a biomarker for human glioma cellularity. J Magn Reson Imaging 2010;31(3):538–548. 10.1002/jmri.22068. [PubMed: 20187195]
23. Farace P, Amelio D, Ricciardi GK, et al. Early MRI changes in glioblastoma in the period between surgery and adjuvant therapy. J Neurooncol 2013;111(2):177–185. 10.1007/s11060-012-0997-y. [PubMed: 23264191]
24. Chang PD, Chow DS, Yang PH, Filippi CG, Lignelli A. Predicting glioblastoma recurrence by early changes in the apparent diffusion coefficient value and signal intensity on FLAIR images. AJR Am J Roentgenol 2017;208(1):57–65. 10.2214/AJR.16.16234. [PubMed: 27726412]
25. Gupta A, Young RJ, Karimi S, et al. Isolated diffusion restriction precedes the development of enhancing tumor in a subset of patients with glioblastoma. AJNR Am J Neuroradiol 2011;32(7):1301–1306. 10.3174/ajnr.A2479. [PubMed: 21596805]
26. Mong S, Ellingson BM, Nghiemphu PL, et al. Persistent diffusion-restricted lesions in bevacizumab-treated malignant gliomas are associated with improved survival compared with matched controls. AJNR Am J Neuroradiol 2012;33(9):1763–1770. 10.3174/ajnr.A3053. [PubMed: 22538078]
27. Yamasaki F, Kurisu K, Aoki T, et al. Advantages of high b-value diffusion-weighted imaging to diagnose pseudo-responses in patients with recurrent glioma after bevacizumab treatment. Eur J Radiol. 2012;81(10):2805 10.1016/j-ejrad.2011.10.018. [PubMed: 22100373]
28. Gerstner ER, Sorensen AG. Diffusion and diffusion tensor imaging in brain cancer. Semin Radiat Oncol 2011;21(2): 141–146. 10.1016/j.semradonc.2010.10.005. [PubMed: 21356481]
29. Abdullah KG, Lubelski D, Nucifora PGP, Brem S. Use of diffusion tensor imaging in glioma resection. Neurosurg Focus 2013;34(4):E1 10.3171/2013.1.FOCUS12412.

30. Lazar M. Mapping brain anatomical connectivity using white matter tractography. NMR Biomed 2010;23:821–835. 10.1002/nbm.1579. [PubMed: 20886567]
31. Wang S, Kim S, Chawla S, et al. Differentiation between glioblastomas and solitary brain metastases using diffusion tensor imaging. NeuroImage 2009;44:653–660. 10.1016/j.neuroimage.2008.09.027. [PubMed: 18951985]
32. Wang S, Martinez-Lage M, Sakai Y, et al. Differentiating tumor progression from pseudoprogression in patients with glioblastomas using diffusion tensor imaging and dynamic susceptibility contrast MRI. Am J Neuroradiol 2016;37:28–36. 10.3174/ajnr.a4474. [PubMed: 26450533]
33. Chawla S, Wang S, Mohan S, et al. Differentiation of brain infection from necrotic glioblastoma using combined analysis of diffusion and perfusion MRI. J Magn Reson Imaging. 2019;49(1):184–194. 10.1002/jmri.26053. [PubMed: 29676844]
34. Wang S, O'Rourke DM, Chawla S, et al. Multiparametric magnetic resonance imaging in the assessment of anti-EGFRvIII chimeric antigen receptor T cell therapy in patients with recurrent glioblastoma. Br J Cancer 2019;120:54–56. 10.1038/s41416-018-0342-0. [PubMed: 30478409]
35. Wang W, Steward CE, Desmond PM. Diffusion tensor imaging in glioblastoma multiforme and brain metastases: The role of p, q, l, and fractional anisotropy. AJNR Am J Neuroradiol. 2009;30(1):203–208. 10.3174/ajnr.A1303. [PubMed: 18842762]
36. Mohan S, Wang S, Coban G, et al. Detection of occult neoplastic infiltration in the corpus callosum and prediction of overall survival in patients with glioblastoma using diffusion tensor imaging. Eur J Radiol 2019;112:106–111. 10.1016/j.ejrad.2019.01.015. [PubMed: 30777198]
37. Wang N, Jain RK, Batchelor TT. New directions in anti-angiogenic therapy for glioblastoma. Neurotherapeutics 2017;14(2):321–332. 10.1007/s13311-016-0510-y. [PubMed: 28083806]
38. Mueller S, Karajannis MA. Pediatric brain tumors — high-grade glioma. Swaiman's pediatric neurology: Amsterdam: Elsevier, Netherlands; 2017 p 979–984. https://linkinghub.elsevier.com/retrieve/pii/B9780323371018001260.
39. Essig M, Shiroishi MS, Nguyen TB, et al. Perfusion MRI: The five most frequently asked technical questions. AJR Am J Roentgenol. 2013;200 (1):24–34. 10.2214/AJR.12.9543. [PubMed: 23255738]
40. Welker K, Boxerman J, Kalnin A, et al. ASFNR recommendations for clinical performance of MR dynamic susceptibility contrast perfusion imaging of the brain. AJNR Am J Neuroradiol. 2015;36(6):E41–E51. 10.3174/ajnr.A4341. [PubMed: 25907520]
41. Ellingson BM, Zaw T, Cloughesy TF, et al. Comparison between intensity normalization techniques for dynamic susceptibility contrast (DSC)-MRI estimates of cerebral blood volume (CBV) in human gliomas. J Magn Reson Imaging 2012;35(6):1472–1477. 10.1002/jmri.23600. [PubMed: 22281731]
42. Leu K, Boxerman JL, Ellingson BM. Effects of MRI protocol parameters, preload injection dose, fractionation strategies, and leakage correction algorithms on the fidelity of dynamic-susceptibility contrast MRI estimates of relative cerebral blood volume in gliomas. American Journal of Neuroradiology 2017;38:478–484. 10.3174/ajnr.a5027. [PubMed: 28034995]
43. Paldino MJ, Barboriak DP. Fundamentals of quantitative dynamic contrast-enhanced MR imaging. Magn Reson Imaging Clin North America 2009;17:277–289. 10.1016/j.mric.2009.01.007.
44. Sourbron SP, Buckley DL. Classic models for dynamic contrast-enhanced MRI. NMR Biomed 2013;26:1004–1027. 10.1002/nbm.2940. [PubMed: 23674304]
45. Verma N, Cowperthwaite MC, Burnett MG, Markey MK. Differentiating tumor recurrence from treatment necrosis: A review of neuro-oncologic imaging strategies. Neuro-Oncology 2013;15:515–534. 10.1093/neuonc/nos307. [PubMed: 23325863]
46. Amukotuwa SA, Yu C, Zaharchuk G. 3D Pseudocontinuous arterial spin labeling in routine clinical practice: A review of clinically significant artifacts. Journal of Magnetic Resonance Imaging 2016;43:11–27. 10.1002/jmri.24873. [PubMed: 25857715]
47. Grade M, Hernandez Tamames JA, Pizzini FB, Achten E, Golay X, Smits M. A neuroradiologist's guide to arterial spin labeling MRI in clinical practice. Neuroradiology 2015;57:1181–1202. 10.1007/s00234-015-1571-z. [PubMed: 26351201]

48. Alsop DC, Detre JA, Golay X, et al. Recommended implementation of arterial spin-labeled perfusion MRI for clinical applications: A consensus of the ISMRM perfusion study group and the European consortium for ASL in dementia. Magn Reson Med 2015;73:102–116. 10.1002/mrm.25197. [PubMed: 24715426]
49. Haller S, Zaharchuk G, Thomas DL, Lovblad K-O, Barkhof F, Golay X. Arterial spin labeling perfusion of the brain: Emerging clinical applications. Radiology 2016;281:337–356. 10.1148/radiol.2016150789. [PubMed: 27755938]
50. £oban G, Mohan S, Kural F, Wang S, O'Rourke DM, Poptani H. Prognostic value of dynamic susceptibility contrast-enhanced and diffusion-weighted MR imaging in patients with Glioblastomas. AJNR Am J Neuroradiol. 2015;36(7):1247–1252. 10.3174/ajnr.A4284. [PubMed: 25836728]
51. BRJ v D, van Laar PJ, Holtman GA, van der Hoorn A. Diagnostic accuracy of magnetic resonance imaging techniques for treatment response evaluation in patients with high-grade glioma, a systematic review and meta-analysis. European Radiology 2017;27:4129–4144. 10.1007/s00330-017-4789-9. [PubMed: 28332014]
52. Wan B, Wang S, Tu M, Wu B, Han P, Xu H. The diagnostic performance of perfusion MRI for differentiating glioma recurrence from pseudoprogression: A meta-analysis. Medicine 2017;96(11):e6333 10.1097/MD.0000000000006333. [PubMed: 28296759]
53. Patel P, Baradaran H, Delgado D, et al. MR perfusion-weighted imaging in the evaluation of high-grade gliomas after treatment: A systematic review and meta-analysis. Neuro Oncol 2017;19(1):118–127. 10.1093/neuonc/now148. [PubMed: 27502247]
54. Seeger A, Braun C, Skardelly M, et al. Comparison of three different MR perfusion techniques and MR spectroscopy for multiparametric assessment in distinguishing recurrent high-grade gliomas from stable disease. Acad Radiol 2013;20:1557–1565. 10.1016/j.acra.2013.09.003. [PubMed: 24200483]
55. Barajas RF, Chang JS, Segal MR, et al. Differentiation of recurrent glioblastoma multiforme from radiation necrosis after external beam radiation therapy with dynamic susceptibility-weighted contrast-enhanced perfusion MR imaging. Radiology 2009;253:486–496. 10.1148/radiol.2532090007. [PubMed: 19789240]
56. Bisdas S, Naegele T, Ritz R, et al. Distinguishing recurrent high-grade gliomas from radiation injury. Acad Radiol 2011;18:575–583. 10.1016/j.acra.2011.01.018. [PubMed: 21419671]
57. Yoo R-E, Choi SH, Kim TM, et al. Dynamic contrast-enhanced MR imaging in predicting progression of enhancing lesions persisting after standard treatment in glioblastoma patients: A prospective study. Eur Radiol 2017;27:3156–3166. 10.1007/s00330-016-4692-9. [PubMed: 27975145]
58. Xu Q, Liu Q, Ge H, et al. Tumor recurrence versus treatment effects in glioma: A comparative study of three dimensional pseudo-continuous arterial spin labeling and dynamic susceptibility contrast imaging. Medicine 2017;96(50):e9332 10.1097/MD.0000000000009332. [PubMed: 29390403]
59. Ozsunar Y, Mullins ME, Kwong K, et al. Glioma recurrence versus radiation necrosis? Acad Radiol 2010;17:282–290. 10.1016/j.acra.2009.10.024. [PubMed: 20060750]
60. Chawla S, Wang S, Wolf RL, et al. Arterial spin-labeling and MR spectroscopy in the differentiation of gliomas. Am J Neuroradiol 2007;28: 1683–1689. 10.3174/ajnr.a0673. [PubMed: 17893221]
61. Chawla S, Oleaga L, Wang S, et al. Role of proton magnetic resonance spectroscopy in differentiating oligodendrogliomas from astrocytomas. J Neuroimaging 2010;20:3–8. 10.1111/j.1552-6569.2008.00307.x. [PubMed: 19021846]
62. Verma G, Chawla S, Mohan S, et al. Three-dimensional echo planar spectroscopic imaging for differentiation of true progression from pseudoprogression in patients with glioblastoma. NMR Biomed 2019; 32:e4042 10.1002/nbm.4042. [PubMed: 30556932]
63. Mohan S, Chawla S, Wang S, et al. Assessment of early response to tumor-treating fields in newly diagnosed glioblastoma using physiologic and metabolic MRI: Initial experience. CNS Oncol 2016;5:137–144. 10.2217/cns-2016-0003. [PubMed: 27076281]

64. Bulik M, Jancalek R, Vanicek J, Skoch A, Mechl M. Potential of MR spectroscopy for assessment of glioma grading. Clin Neurol Neurosurg 2013;115(2):146–153. 10.1016/j.clineuro.2012.11.002. [PubMed: 23237636]
65. Poptani H, Gupta RK, Jain VK, Roy R, Pandey R. Cystic intracranial mass lesions: Possible role of in vivo MR spectroscopy in its differential diagnosis. Magn Reson Imaging 1995;13:1019–1029. 10.1016/0730-725x(95)00045-i. [PubMed: 8583866]
66. Parra NA, Andres Parra N, Maudsley AA, et al. Volumetric spectroscopic imaging of glioblastoma multiforme radiation treatment volumes. Int J Radiat Oncol Biol Phys 2014;90:376–384. 10.1016/j.ijrobp.2014.03.049. [PubMed: 25066215]
67. Lin DDM, Lin Y, Link K, et al. Echoplanar magnetic resonance spectroscopic imaging before and following radiation therapy in patients with high-grade glioma. Int J Radiat Oncol Biol Phys 2016;96(2S):E133–E134. 10.1016/jjjrobp.2016.06.926.
68. Shim H, Holder CA, Olson JJ. Magnetic resonance spectroscopic imaging in the era of pseudoprogression and pseudoresponse in glioblastoma patient management. CNS Oncology 2013;2:393–396. 10.2217/cns.13.39. [PubMed: 25054660]
69. Chawla S, Wang S, Kim S, et al. Radiation injury to the normal brain measured by 3D-echo-planar spectroscopic imaging and diffusion tensor imaging: Initial experience. J Neuroimaging 2015;25(1):97–104. 10.1111/jon.12070. [PubMed: 24279509]
70. Zhu H, Barker PB. MR spectroscopy and spectroscopic imaging of the brain. Methods Mol Biol 2011;711:203–226. 10.1007/978-1-61737-992-5_9. [PubMed: 21279603]
71. Glunde K, Bhujwalla ZM, Ronen SM. Choline metabolism in malignant transformation. Nat Rev Cancer 2011;11:835–848. 10.1038/nrc3162. [PubMed: 22089420]
72. Chawla S, Lee S-C, Mohan S, et al. Lack of choline elevation on proton magnetic resonance spectroscopy in grade I-III gliomas. Neuroradiol J 2019;32(4):250–258. 10.1177/1971400919846509. [PubMed: 31050313]
73. Warburg O. On the origin of cancer cells. Science 1956;123:309–314. 10.1126/science.123.3191.309. [PubMed: 13298683]
74. Delikatny EJ, Chawla S, Leung D-J, Poptani H. MR-visible lipids and the tumor microenvironment. NMR Biomed 2011;24(6):592–611. 10.1002/nbm.1661. [PubMed: 21538631]
75. Remy C, Arus C, Ziegler A, et al. In vivo, ex vivo, and in vitro one- and two-dimensional nuclear magnetic resonance spectroscopy of an intracerebral glioma in rat brain: Assignment of resonances. J Neurochem 2008;62:166–179. 10.1046/j-1471-4159.1994.62010166.x.
76. DeBerardinis RJ, Mancuso A, Daikhin E, et al. Beyond aerobic glycolysis: Transformed cells can engage in glutamine metabolism that exceeds the requirement for protein and nucleotide synthesis. Proc Natl Acad Sci 2007;104:19345–19350. 10.1073/pnas.0709747104. [PubMed: 18032601]
77. Choi C, Ganji SK, DeBerardinis RJ, et al. 2-hydroxyglutarate detection by magnetic resonance spectroscopy in IDH-mutated patients with gliomas. Nat Med 2012;18:624–629. 10.1038/nm.2682. [PubMed: 22281806]
78. Verma G, Mohan S, Nasrallah MP, et al. Non-invasive detection of 2-hydroxyglutarate in IDH-mutated gliomas using two-dimensional localized correlation spectroscopy (2D L-COSY) at 7 Tesla. J Transl Med 2016;14:274 10.1186/s12967-016-1035-1. [PubMed: 27659543]
79. Chernov MF, Ono Y, Abe K, et al. Differentiation of tumor progression and radiation-induced effects after intracranial radiosurgery. Acta Neurochir Suppl 2013;116:193–210. 10.1007/978-3-7091-1376-9_29. [PubMed: 23417479]
80. Zhang H, Ma L, Wang Q, Zheng X, Wu C, Xu B-N. Role of magnetic resonance spectroscopy for the differentiation of recurrent glioma from radiation necrosis: A systematic review and meta-analysis. Eur J Radiol 2014;83:2181–2189. 10.1016/j.ejrad.2014.09.018. [PubMed: 25452098]
81. Sawlani V, Taylor R, Rowley K, Redfern R, Martin J, Poptani H. Magnetic resonance spectroscopy for differentiating pseudo-progression from true progression in GBM on concurrent chemoradiotherapy. Neuroradiol J 2012, 575;25:575–586. 10.1177/197140091202500511.
82. Maudsley AA, Gupta RK, Stoyanova R, et al. Mapping of glycine distributions in gliomas. Am J Neuroradiol 2014;35:S31–S36. 10.3174/ajnr.a3845. [PubMed: 24481330]
83. van PCM Z, Yadav NN. Chemical exchange saturation transfer (CEST): What is in a name and what isn't? Magn Reson Med 2011;65:927–948. 10.1002/mrm.22761. [PubMed: 21337419]

84. Zhou J, Payen J-F, Wilson DA, Traystman RJ, van PCM Z. Using the amide proton signals of intracellular proteins and peptides to detect pH effects in MRI. Nat Med 2003;9:1085–1090. 10.1038/nm907. [PubMed: 12872167]
85. Ma B, Blakeley JO, Hong X, et al. Applying amide proton transfer-weighted MRI to distinguish pseudoprogression from true progression in malignant gliomas. J Magn Reson Imaging 2016;44(2):456–462. 10.1002/jmri.25159. [PubMed: 26788865]
86. Isobe T, Matsumura A, Anno I, et al. Quantification of cerebral metabolites in glioma patients with proton MR spectroscopy using T2 relaxation time correction. Magn Reson Imaging 2002;20:343–349. 10.1016/s0730-725x(02)00500–3. [PubMed: 12165353]
87. Zhou J, Heo H-Y, Knutsson L, van Zijl PCM, Jiang S. APT-weighted MRI: Techniques, current neuro applications, and challenging issues. J Magn Reson Imaging. 2019;50(2):347–364. 10.1002/jmri.26645. [PubMed: 30663162]
88. Zhou J, Tryggestad E, Wen Z, et al. Differentiation between glioma and radiation necrosis using molecular magnetic resonance imaging of endogenous proteins and peptides. Nat Med 2011;17(1):130–134. 10.1038/nm.2268. [PubMed: 21170048]
89. de Groot J, de Groot J, Sontheimer H. Glutamate and the biology of gliomas. Glia 2011;59:1181–1189. 10.1002/glia.21113. [PubMed: 21192095]
90. Likavcanova K, Dobrota D, Liptaj T, et al. In vitro study of astrocytic tumour metabolism by proton magnetic resonance spectroscopy. Gen Physiol Biophys 2005;24(3):327–335. https://www.ncbi.nlm.nih.gov/pubmed/16308427. [PubMed: 16308427]
91. Bouzier A-K, Quesson B, Valeins H, Canioni P, Merle M. [1–13C]Glucose metabolism in the tumoral and nontumoral cerebral tissue of a glioma-bearing rat. J Neurochem 2002;72:2445–2455. 10.1046/j.1471-4159.1999.0722445.x.
92. Ye Z-C, Rothstein JD, Sontheimer H. Compromised glutamate transport in human glioma cells: reduction—Mislocalization of sodium-dependent glutamate transporters and enhanced activity of cystine-glutamate exchange. J Neurosci 1999;19:10767–10777. 10.1523/jneurosci.19-24-10767.1999. [PubMed: 10594060]
93. Mittal S, Barkmeier D, Hua J, et al. Intracranial EEG analysis in tumor-related epilepsy: Evidence of distant epileptic abnormalities. Clin Neurophysiol 2016;127(1):238–244. 10.1016/j.clinph.2015.06.028. [PubMed: 26493495]
94. Cai K, Haris M, Singh A, et al. Magnetic resonance imaging of glutamate. Nat Med 2012;18:302–306. 10.1038/nm.2615. [PubMed: 22270722]
95. Neal A, Moffat BA, Stein JM, et al. Glutamate weighted imaging contrast in gliomas with 7 Tesla magnetic resonance imaging. Neuroimage Clin 2019;22:101694. 10.1016/j.nicl.2019.101694.
96. Chen XZ, Yin XM, Ai L, Chen Q, Li SW, Dai JP. Differentiation between brain glioblastoma multiforme and solitary metastasis: Qualitative and quantitative analysis based on routine MR imaging. AJNR Am J Neuroradiol. 2012;33(10):1907–1912. 10.3174/ajnr.A3106. [PubMed: 22743640]
97. Nael K, Bauer AH, Hormigo A, et al. Multiparametric MRI for differentiation of radiation necrosis from recurrent tumor in patients with treated glioblastoma. AJR Am J Roentgenol. 2018;210(1):18–23. 10.2214/AJR.17.18003. [PubMed: 28952810]
98. Li C, Wang S, Yan J-L, et al. Characterizing tumor invasiveness of glioblastoma using multiparametric magnetic resonance imaging. J Neurosurg 2019;26:1–8. 10.3171/2018.12.JNS182926.
99. Stringfield O, Arrington JA, Johnston SK, et al. Multiparameter MRI predictors of long-term survival in glioblastoma multiforme. Tomography 2019;5(1):135–144. 10.18383/j.tom.2018.00052. [PubMed: 30854451]
100. Huang RY, Neagu MR, Reardon DA, Wen PY. Pitfalls in the neuroimaging of glioblastoma in the RRA of antiangiogenic and immuno/targeted therapy detecting illusive disease, defining response. Frontiers in Neurology 2015;6:33 10.3389/fneur.2015.00033. [PubMed: 25755649]
101. Rudie JD, Rauschecker AM, Bryan RN, Davatzikos C, Mohan S. Emerging applications of artificial intelligence in neuro-oncology. Radiology 2019;290(3):607–618. 10.1148/radiol.2018181928. [PubMed: 30667332]

102. McBee MP, Awan OA, Colucci AT, et al. Deep learning in radiology. Acad Radiol 2018;25(11):1472–1480. 10.1016/j.acra.2018.02.018. [PubMed: 29606338]
103. Sotoudeh H, Shafaat O, Bernstock JD, et al. Artificial intelligence in the management of glioma: Era of personalized medicine. Front Oncol 2019;9:768 10.3389/fonc.2019.00768. [PubMed: 31475111]
104. Li-Chun Hsieh K, Chen C-Y, Lo C-M. Quantitative glioma grading using transformed gray-scale invariant textures of MRI. Comput Biol Med 2017;83:102–108. 10.1016/j.compbiomed.2017.02.012. [PubMed: 28254615]
105. Wu J, Qian Z, Tao L, et al. Resting state fMRI feature-based cerebral glioma grading by support vector machine. Int J Comput Assist Radiol Surg 2015;10(7): 1167–1174. 10.1007/s11548-014-1111-z. [PubMed: 25227532]
106. Tian Q, Yan L-F, Zhang X, et al. Radiomics strategy for glioma grading using texture features from multiparametric MRI. J Magn Reson Imaging. 2018;48(6):1518–1528. 10.1002/jmri.26010. [PubMed: 29573085]
107. Mao Y, Liao W, Cao D, et al. An artificial neural network model for glioma grading using image information. Zhong Nan Da Xue Xue Bao Yi Xue Ban 2018;43(12):1315–1322. 10.11817/jjssn.1672-7347.2018.12.006. [PubMed: 30643047]
108. Sonoda Y, Shibahara I, Kawaguchi T, et al. Association between molecular alterations and tumor location and MRI characteristics in anaplastic gliomas. Brain Tumor Pathol 2015;32(2):99–104. 10.1007/s10014-014-0211-3. [PubMed: 25537428]
109. Zhou M, Scott J, Chaudhury B, et al. Radiomics in brain tumor: Image assessment, quantitative feature descriptors, and machine-learning approaches. AJNR Am J Neuroradiol. 2018;39(2):208–216. 10.3174/ajnr.A5391. [PubMed: 28982791]
110. Chang K, Bai HX, Zhou H, et al. Residual convolutional neural network for the determination of status in low- and high-grade gliomas from MR imaging. Clin Cancer Res 2018;24(5):1073–1081. 10.1158/1078-0432.CCR-17-2236. [PubMed: 29167275]
111. Wu S, Meng J, Yu Q, Li P, Fu S. Radiomics-based machine learning methods for isocitrate dehydrogenase genotype prediction of diffuse gliomas. J Cancer Res Clin Oncol 2019;145(3):543–550. 10.1007/s00432-018-2787-1. [PubMed: 30719536]
112. Zhang B, Chang K, Ramkissoon S, et al. Multimodal MRI features predict isocitrate dehydrogenase genotype in high-grade gliomas. Neuro Oncol. 2017;19(1):109–117. 10.1093/neuonc/now121. [PubMed: 27353503]
113. Li Z, Wang Y, Yu J, Guo Y, Cao W. Deep Learning based Radiomics (DLR) and its usage in noninvasive IDH1 prediction for low grade glioma. Sci Rep 2017;7(1):5467 10.1038/s41598-017-05848-2. [PubMed: 28710497]
114. Korfiatis P, Kline TL, Lachance DH, Parney IF, Buckner JC, Erickson BJ. Residual deep convolutional neural network predicts MGMT methylation status. J Digital Imaging 2017;30:622–628. 10.1007/s10278-017-0009-z.
115. Han L, Kamdar MR. MRI to MGMT: Predicting methylation status in glioblastoma patients using convolutional recurrent neural networks. Biocomputing 2018;2018:331–342. 10.1142/9789813235533_0031.
116. Chang P, Grinband J, Weinberg BD, et al. Deep-learning convolutional neural networks accurately classify genetic mutations in gliomas. American Journal of Neuroradiology 2018;39:1201–1207. 10.3174/ajnr.a5667. [PubMed: 29748206]
117. Lotan E, Jain R, Razavian N, Fatterpekar GM, Lui YW. State of the art: Machine learning applications in glioma imaging. AJR Am J Roentgenol. 2019;212(1):26–37. 10.2214/AJR.18.20218. [PubMed: 30332296]
118. Vasudevan P, Murugesan T. Cancer subtype discovery using prognosis-enhanced neural network classifier in multigenomic data. Technol Cancer Res Treat 2018;1(17):1533033818790509. 10.1177/1533033818790509.
119. LeCun Y, Bengio Y, Hinton G. Deep learning. Nature 2015;521(7553): 436–444. 10.1038/nature14539. [PubMed: 26017442]
120. Litjens G, Kooi T, Bejnordi BE, et al. A survey on deep learning in medical image analysis. Med Image Anal 2017;42:60–88. 10.1016/j.media.2017.07.005. [PubMed: 28778026]

121. Blanc-Durand P, Van Der Gucht A, Schaefer N, Itti E, Prior JO. Automatic lesion detection and segmentation of 18F-FET PET in gliomas: A full 3D U-Net convolutional neural network study. PLoS One 2018; 13(4):e0195798. 10.1371/journal.pone.0195798.
122. Tustison NJ, Shrinidhi KL, Wintermark M, et al. Optimal symmetric multimodal templates and concatenated random forests for supervised brain tumor segmentation (simplified) with ANTsR. Neuroinformatics 2015;13(2):209–225. 10.1007/s12021-014-9245-2. [PubMed: 25433513]
123. Pereira S, Pinto A, Alves V, Silva CA. Brain tumor segmentation using convolutional neural networks in MRI images. IEEE Trans Med Imaging 2016;35(5):1240–1251. 10.1109/TMI.2016.2538465. [PubMed: 26960222]
124. Havaei M, Davy A, Warde-Farley D, et al. Brain tumor segmentation with deep neural networks. Med Image Anal 2017;35:18–31. 10.1016/j.media.2016.05.004. [PubMed: 27310171]
125. Kamnitsas K, Ledig C, Newcombe VFJ, et al. Efficient multi-scale 3D CNN with fully connected CRF for accurate brain lesion segmentation. Med Image Anal 2017;36:61–78. 10.1016/j.media.2016.10.004. [PubMed: 27865153]
126. Cui S, Mao L, Jiang J, Liu C, Xiong S. Automatic semantic segmentation of brain gliomas from MRI images using a deep cascaded neural network. J Healthcare Eng 2018;2018:4940593. 10.1155/2018/4940593.
127. Fabelo H, Halicek M, Ortega S, et al. Deep learning-based framework for in vivo identification of glioblastoma tumor using hyperspectral images of human brain. Sensors 2019;19:920 10.3390/s19040920.
128. Rodenacker K, Bengtsson E. A feature set for cytometry on digitized microscopic images. Anal Cell Pathol 2003;25(1):1–36. 10.1155/2003/548678. [PubMed: 12590175]
129. Marchevsky AM, Wick MR. Evidence-based medicine, medical decision analysis, and pathology. Hum Pathol 2004;35(10):1179–1188. 10.1016/j.humpath.2004.06.004. [PubMed: 15492984]
130. Fukuma K, Prasath VBS, Kawanaka H, Aronow BJ, Takase H. A study on nuclei segmentation, feature extraction and disease stage classification for human brain histopathological images. Procedia Comput Sci 2016;96:1202–1210. https://linkinghub.elsevier.com/retrieve/pii/S1877050916319743.
131. Yonekura A, Kawanaka H, Prasath VBS, Aronow BJ, Takase H. Automatic disease stage classification of glioblastoma multiforme histopathological images using deep convolutional neural network. Biomed Eng Lett 2018;8(3):321–327. 10.1007/s13534-018-0077-0. [PubMed: 30603216]
132. Wang X, Wang D, Yao Z, et al. Machine learning models for multiparametric glioma grading with quantitative result interpretations. Front Neurosci 2018;12:1046 10.3389/fnins.2018.01046. [PubMed: 30686996]
133. Hu X, Wong KK, Young GS, Guo L, Wong ST. Support vector machine multiparametric MRI identification of pseudoprogression from tumor recurrence in patients with resected glioblastoma. J Magn Reson Imaging 2011;33(2):296–305. 10.1002/jmri.22432. [PubMed: 21274970]
134. Sarkiss CA, Germano IM. Machine learning in neuro-oncology: Can data analysis from 5,346 patients change decision making paradigms? World Neurosurg 2019;124:287–294. 10.1016/j.wneu.2019.01.046.
135. Nie D, Lu J, Zhang H, et al. Multi-channel 3D deep feature learning for survival time prediction of brain tumor patients using multi-modal neuroimages. Sci Rep 2019;9(1):1103 10.1038/s41598-018-37387-9. [PubMed: 30705340]
136. Hao J, Kim Y, Kim T-K, Kang M. PASNet: Pathway-associated sparse deep neural network for prognosis prediction from high-throughput data. BMC Bioinformatics 2018;19(1):510 10.1186/s12859-018-2500-z. [PubMed: 30558539]
137. Emblem KE, Pinho MC, Zöllner FG, et al. A generic support vector machine model for preoperative glioma survival associations. Radiology 2015;275(1):228–234. 10.1148/radiol.14140770. [PubMed: 25486589]
138. Lao J, Chen Y, Li Z-C, et al. A deep learning-based radiomics model for prediction of survival in Glioblastoma Multiforme. Sci Rep 2017;7 (1):10353 10.1038/s41598-017-10649-8. [PubMed: 28871110]

**CME Information: Emerging MR Imaging Techniques to Redefine Treatment Response in Patients with Glioblastoma**

If you wish to receive credit for this activity, please refer to the website: www.wileyhealthlearning.com/JMRI

**Educational Objectives**

Upon completion of this educational activity, participants will be better able to:

- Describe the utility of advanced neuroimaging techniques such as diffusion imaging, perfusion imaging, proton magnetic resonance spectroscopy, and chemical exchange saturation transfer in characterizing and evaluating treatment response in patients with glioblastoma.
- Discuss existing challenges and limitations of these techniques in clinical settings and possible solutions to avoiding pitfalls in study design, data acquisition, and analysis in future studies.

**Activity Disclosures**

No commercial support has been accepted related to the development or publication of this activity.

**Faculty Disclosures**

**Editor-in-Chief:** Mark E. Schweitzer, MD, discloses no relevant financial relationships.

**CME Editor:** Mustafa R. Bashir, MD, discloses grants from CymaBay, Madrigal Pharmaceuticals, Metacrine, NGM and Pinnacle, institutional support from Clinical Research, ProSciento, and Siemens as principal investigator, and consultant fees from MedPace.

**Authors:**

The authors reported no conflicts of interest or financial relationships relevant to this article.

This activity underwent peer review in line with the standards of editorial integrity and publication ethics. Conflicts of interest have been identified and resolved in accordance with John Wiley and Sons, Inc.'s Policy on Activity Disclosure and Conflict of Interest.

**Accreditation**

John Wiley and Sons, Inc. is accredited by the Accreditation Council for Continuing Medical Education to provide continuing medical education for physicians.

John Wiley and Sons, Inc. designates this journal-based CME activity for a maximum of 1.0 *AMA PRA Category 1 Credit*™. Physicians should only claim credit commensurate with the extent of their participation in the activity.

For information on applicability and acceptance of continuing medical education credit for this activity, please consult your professional licensing board.

This activity is designed to be completed within 1 hour. To successfully earn credit, participants must complete the activity during the valid credit period, which is up to two years from initial publication. Additionally, up to 3 attempts and a score of 70% or better is needed to pass the post test.

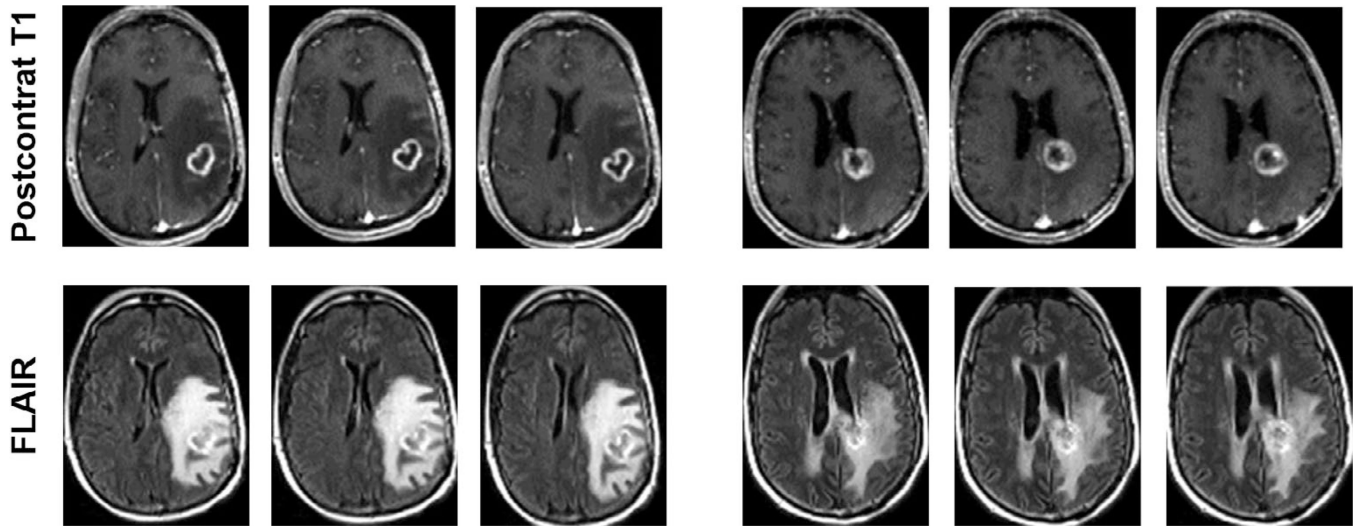


**FIGURE 1:**

Postcontrast $T_1$-weighted and $T_2$-FLAIR images at three different slice levels from patients with TP (left panel) and PsP (right panel) demonstrating equivocal imaging findings with similar patterns of contrast enhancement and surrounding areas of $T_2$-FLAIR signal abnormality suggesting the limitation of conventional MR imaging in reliably differentiating TP from PsP in GBM patients.

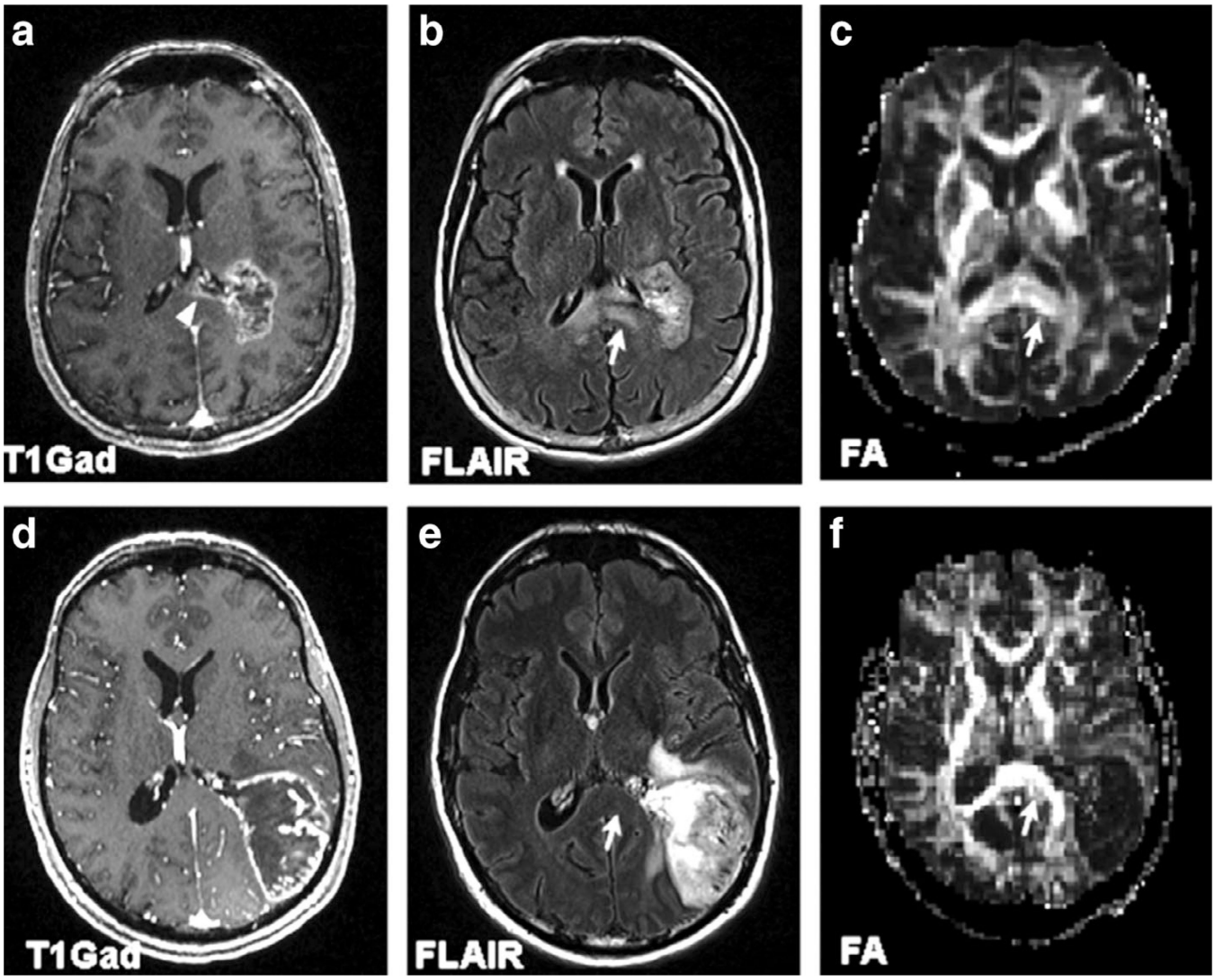


**FIGURE 2:**

MR images of 70-year-old female glioblastoma patient with corpus callosum invasion (top panel) (a–c) and a 53-year-old male glioblastoma patient without corpus callosum invasion (bottom panel) (d–f). Axial contrast-enhanced $T_1$-weighted images (a,d) demonstrate the extension of enhancing tumor into the splenium of CC in (a) (arrowhead), with normal-appearing CC in (d). Axial FLAIR images (b,e) demonstrate corresponding expansile infiltrative FLAIR signal abnormality in the splenium of corpus callosum (arrow) in (b), whereas the CC seems uninvolved in (e, arrow). Lower FA from the splenium of the corpus callosum is noticed in the FA map (c, arrow) for the patient with shorter survival than the one with longer overall survival (f, arrow). Reprinted with permission from Ref. 39 (Mohan et al., Eur J Radiol 2019 Mar; 112:106–111).

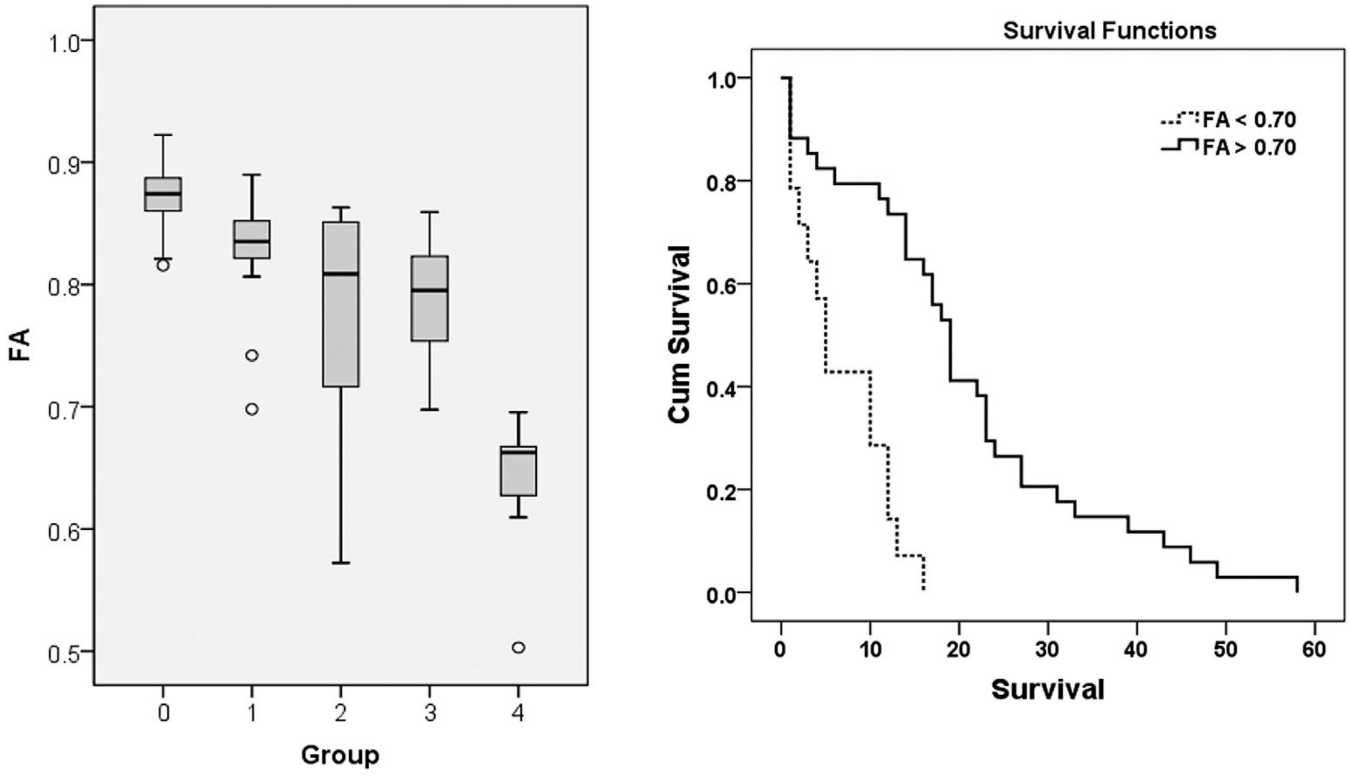


**FIGURE 3:**

Left panel: Boxplot of FA from the corpus callosum (CC) in GBM patients with short and long survival. The solid line inside the box represents the median value, while the edges represent the 25$^{th}$ and 75$^{th}$ percentiles. Straight line (bars) on each box indicates the range of data distribution. Circles represent outliers (values more than 1.5 box length from the 75th/25th percentile). 0. Control group.1. Long survivors without CC invasion. 2. Short survivors without CC invasion. 3. Long survivors with CC invasion. 4. Short survivors with CC invasion. Comparison between groups 1 and 2 ($P = 0.14$), groups 2 and 3 ($P = 0.95$) did not reach a significant difference. There were significant differences between all other groups ($P < 0.05$). Right panel: The ROC curve demonstrates that the FA value from the CC is the best predictor for overall survival, with an AUC of 0.77, sensitivity 1, specificity 0.59 using a cutoff value of 0.70). Reprinted with permission from Ref, 39 (Mohan et al., Eur J Radiol 2019 Mar; 112:106–111).

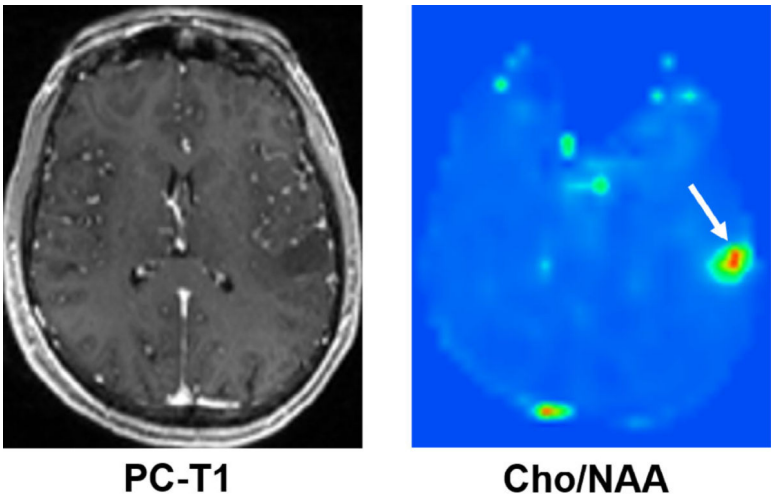


**FIGURE 4:**

Axial postcontrast $T_1$-weighted image demonstrating a nonenhancing neoplasm in the left parietal lobe; however, the corresponding 3D-EPSI derived metabolite ratio map demonstrates high Cho/NAA, suggesting a higher-grade glioma. On histopathology (not shown), this neoplasm showed areas of increased mitotic activities and pseudopalisading necrosis consistent with GBM (WHO grade IV).

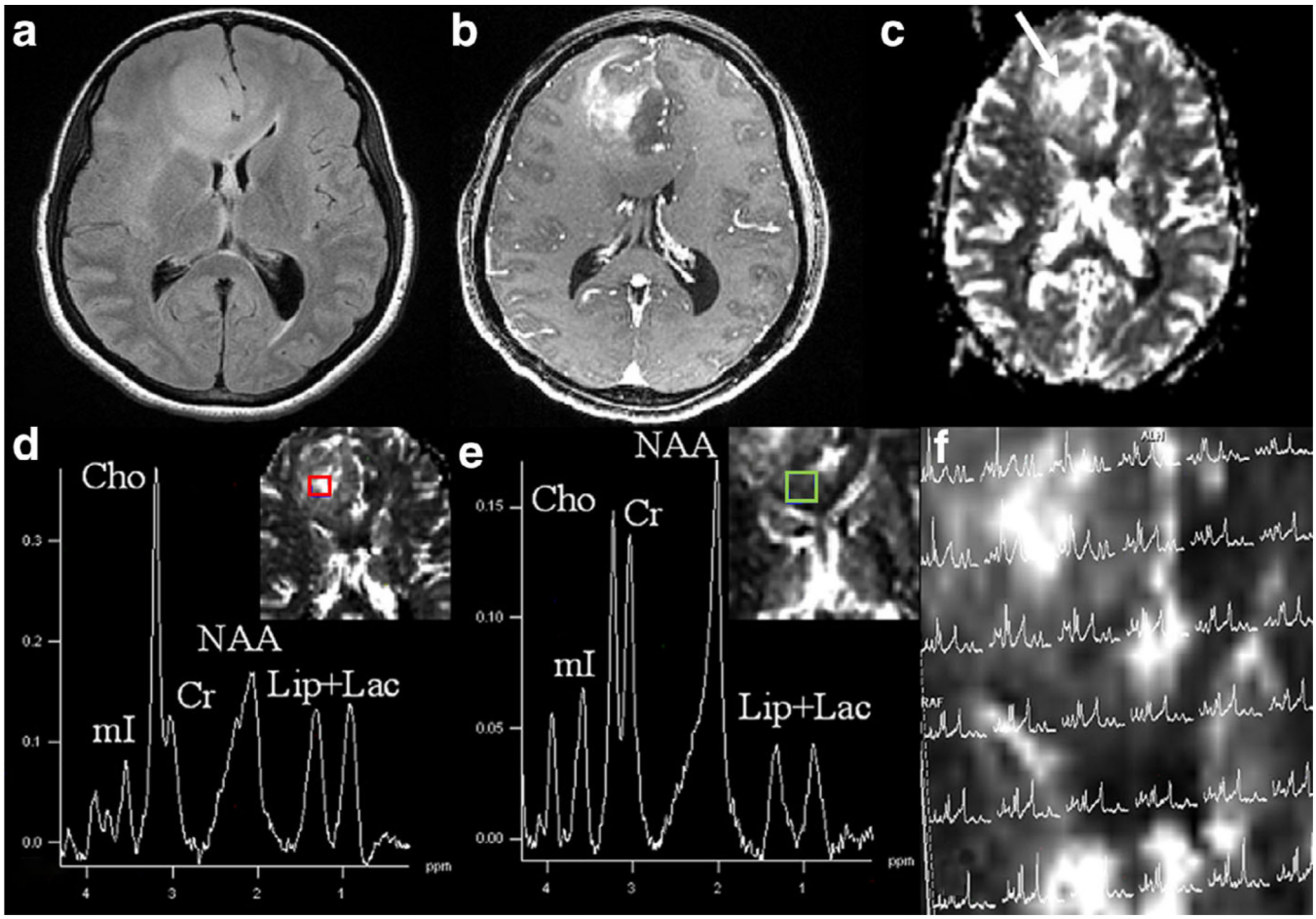


**FIGURE 5:**

Axial $T_2$-FLAIR image (a) demonstrating an ill-defined hyperintense and expansile mass in the right frontal region extending into the genu of CC. There is heterogeneous contrast enhancement within the mass on the corresponding postcontrast $T_1$-weighted image (b). A DSC-derived CBV map (c) shows high CBV within the mass. Proton MR spectra (d,e) from a voxel encompassing a high CBV region (red color) and from a voxel encompassing a low CBV region (green color) are exhibiting various metabolites. Please note the presence of high Cho levels from a high CBV region within the neoplasm, suggesting regions of high vascularity are associated with increased cellular proliferation. $^1$H MRS grid overlaid on CBV map (e) showing spectra from different regions of neoplasm. On histopathology (not shown), this mass showed areas of high cellularity, pseudopalisading necrosis, and endothelial proliferation consistent with anaplastic astrocytoma (WHO grade III).

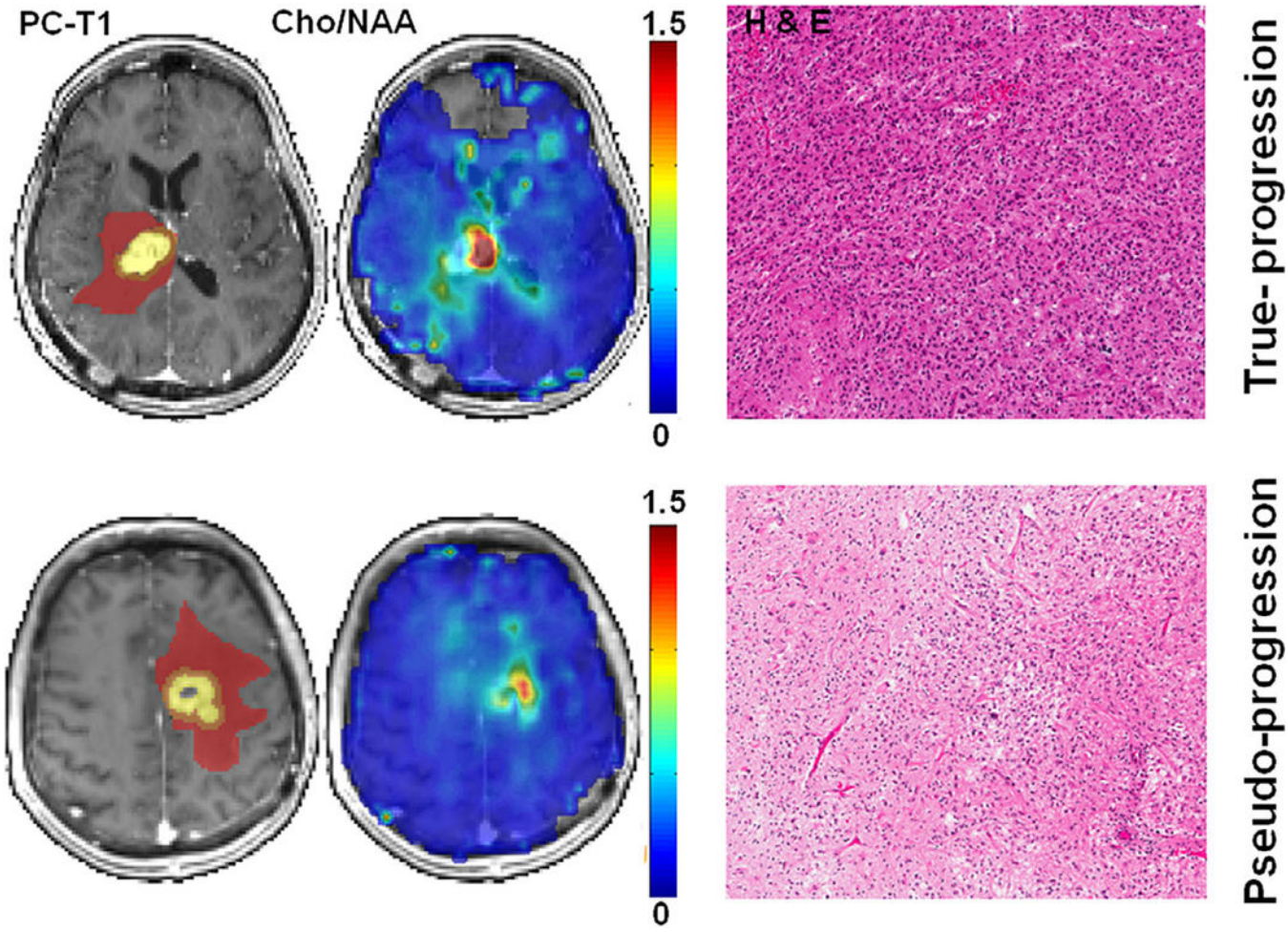


**FIGURE 6:**

Top row: axial postcontrast $T_1$-weighted image from a patient with TP, demonstrating a neoplasm in the right thalamus infiltrating into the lateral ventricles. The ROIs are overlaid on the image, with the colors indicating the following defined regions: yellow, CER; orange, IPR; brown, DPR. The corresponding Cho/NAA map shows areas of elevated Cho/NAA (color bar indicating the distribution of nonnormalized Cho/NAA). A photomicrograph of a histologic section (hematoxylin-eosin stain) shows zones of high tumor cellularity, necrosis, and vascular proliferation. Bottom row: axial postcontrast $T_1$-weighted image from a patient with PsP, demonstrating a neoplasm in the left frontal lobe. The different ROIs as defined above, are overlaid on the image. The corresponding Cho/NAA map shows reduced Cho/NAA compared with that of the TP case shown above. A photomicrograph of hematoxylin-eosin stain reveals most of the tissue with treatment-related changes, including extensive geographic necrosis and vascular fibrinoid necrosis. Reprinted with permission from Ref. 62 (Verma et al., NMR Biomed 2019 Feb; 32 (2): e4042).

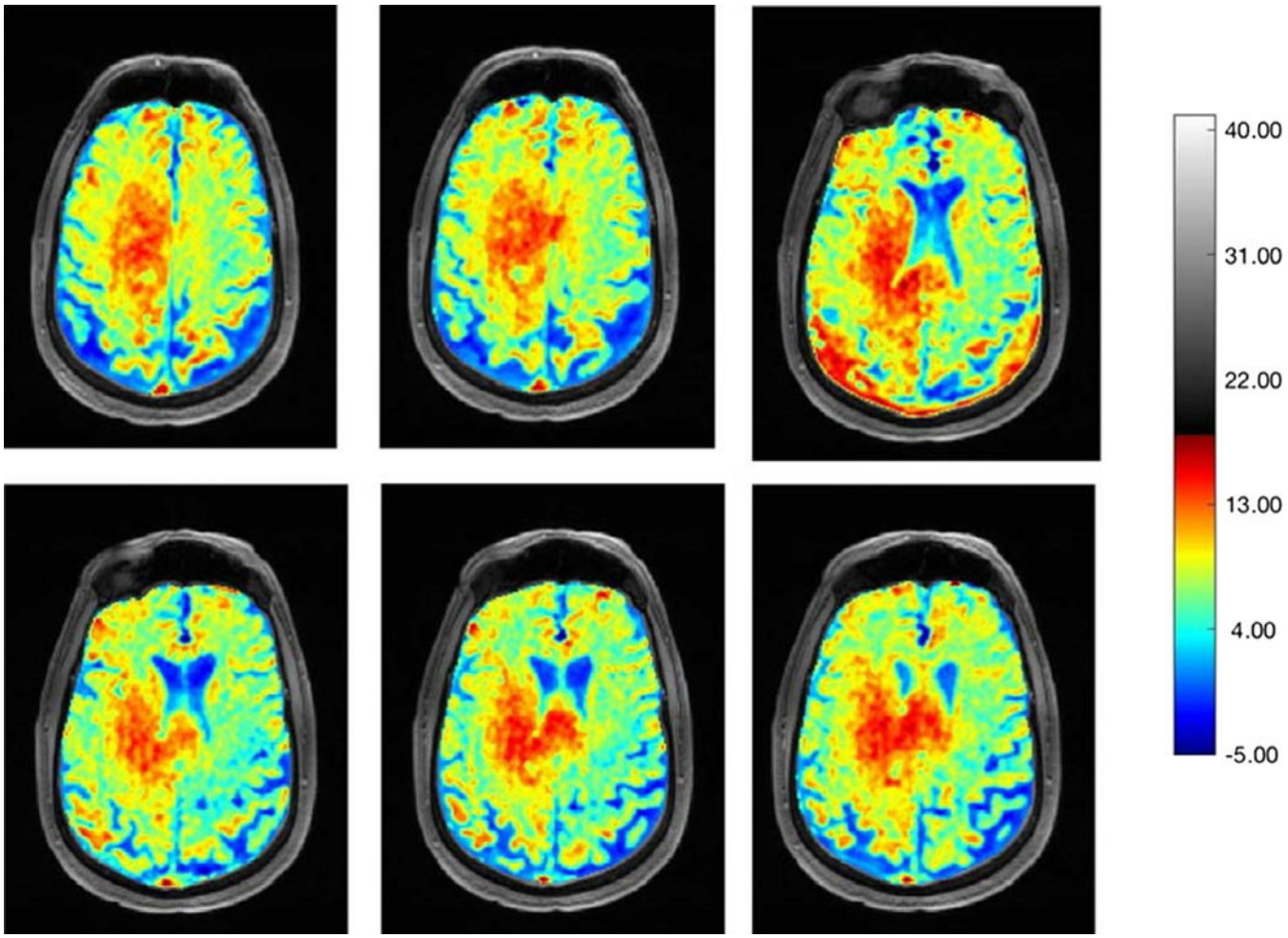


**FIGURE 7:**

Representative $B_0$ and $B_1$ field in-homogeneity corrected Glu-CEST maps at different slice levels demonstrating high glutamate contents within the tumor bed. Please note the presence of high glutamate signals in the body and splenium of corpus callosum, indicating infiltrative nature of this neoplasm.

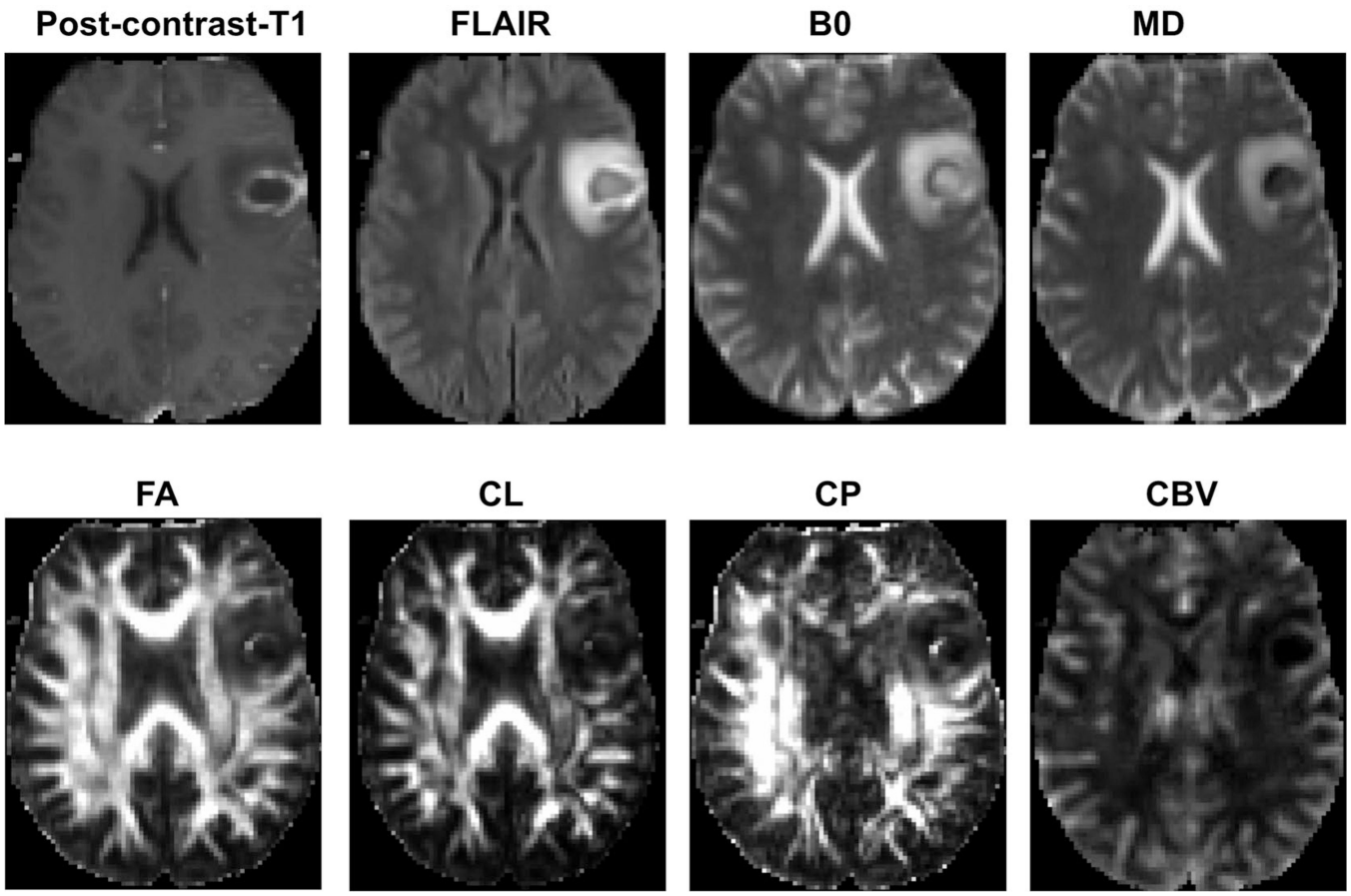


**FIGURE 8:**

A patient with pyogenic abscess. An axial postcontrast $T_1$-weighted image demonstrating a ring-enhancing lesion in the left frontal lobe. This lesion demonstrates heterogeneous signal intensities on the corresponding $T_2$-FLAIR and $B_0$ images, with moderate edema. The central core of the lesion shows low signal on the MD map, and slightly high signal intensities on the FA and CP maps, indicating anisotropic content. An enhancing region in the abscess wall demonstrates minimally elevated rCBV. Reprinted with permission from Ref. 36 (Chawla et al., J Magn Reson Imaging2019 Jan; 49 (1):184–194).

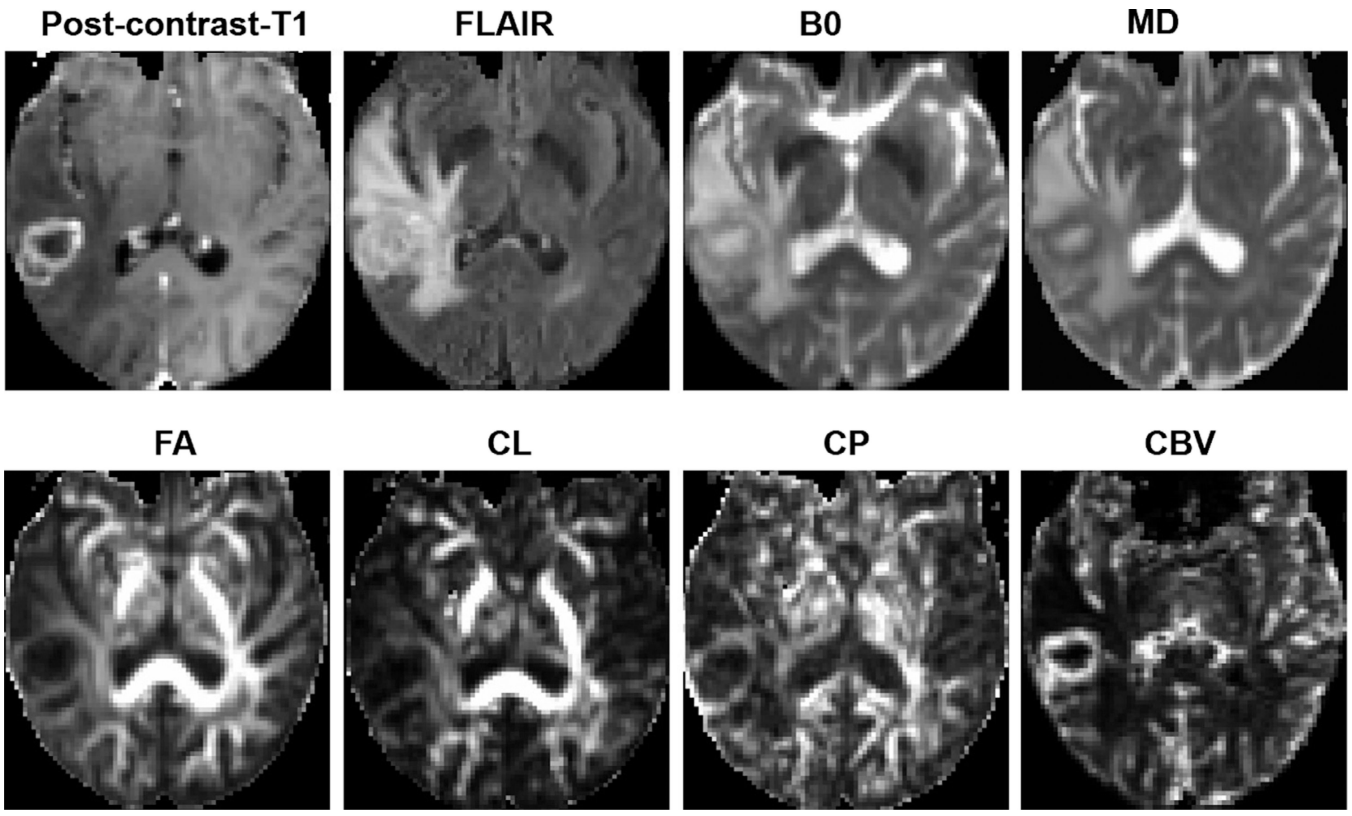


**FIGURE 9:**

A patient with necrotic GBM. Axial postcontrast $T_1$-weighted image demonstrates a ring-enhancing lesion in the right posterior temporal lobe, with heterogeneous signal intensities on the corresponding $T_2$-FLAIR and $B_0$ images as well as marked surrounding edema. The central core of the lesion shows high MD and low FA, CL, and CP. Also, marked elevation of rCBV corresponding to the enhancing region is visible. Reprinted with permission from Ref. 36 (Chawla et al., J Magn Reson Imaging 2019 Jan; 49 (1):184–194).

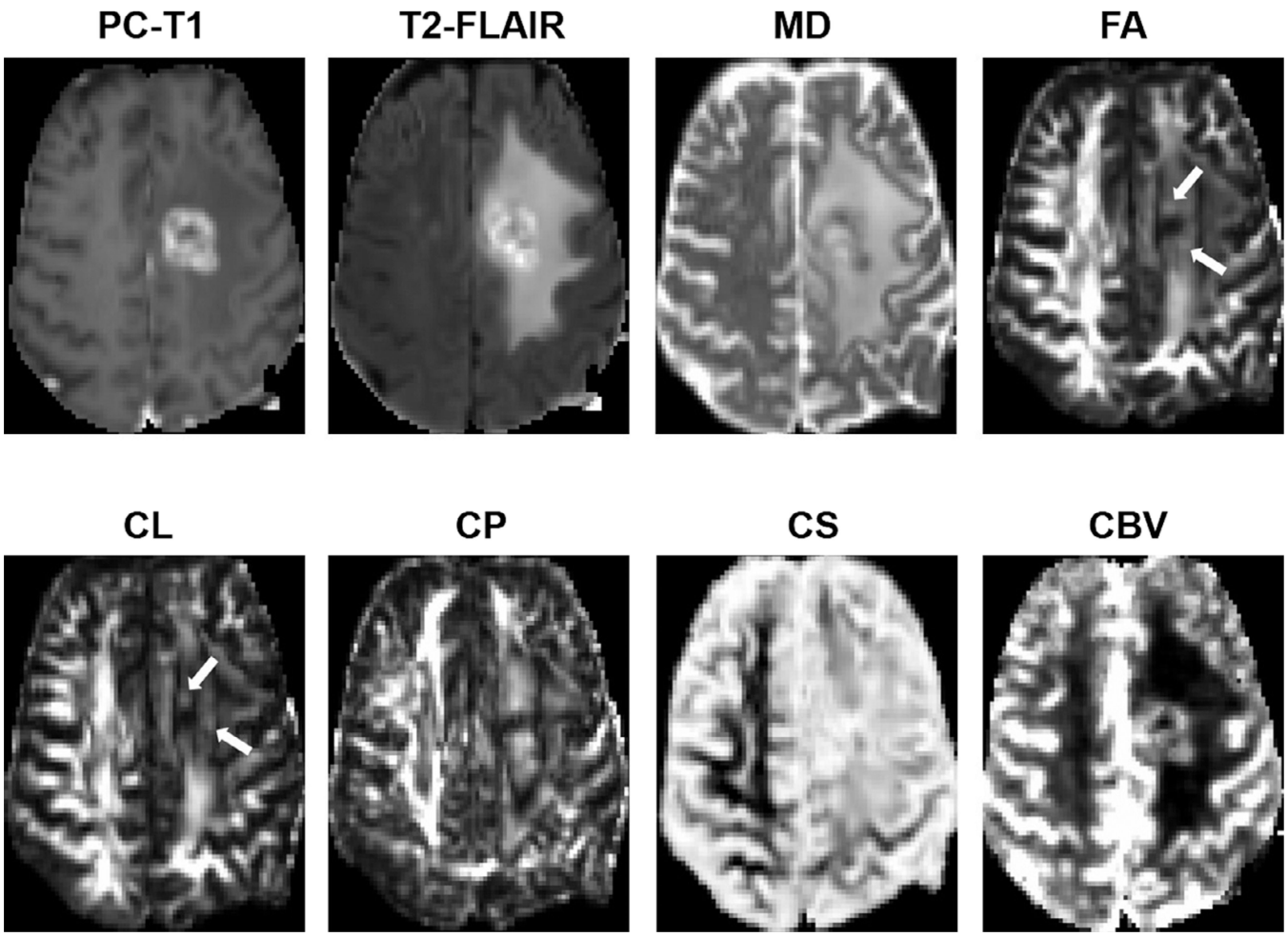


**FIGURE 10:**

Axial MR images from a 62-year-old patient with TP. Postcontrast $T_1$-weighted image shows an enhancing lesion in the left frontal lobe. Coregistered DTI-derived parametric maps and CBV maps are shown. Increased FA, CL, and CBV are seen corresponding to the areas of enhancement (white arrows).

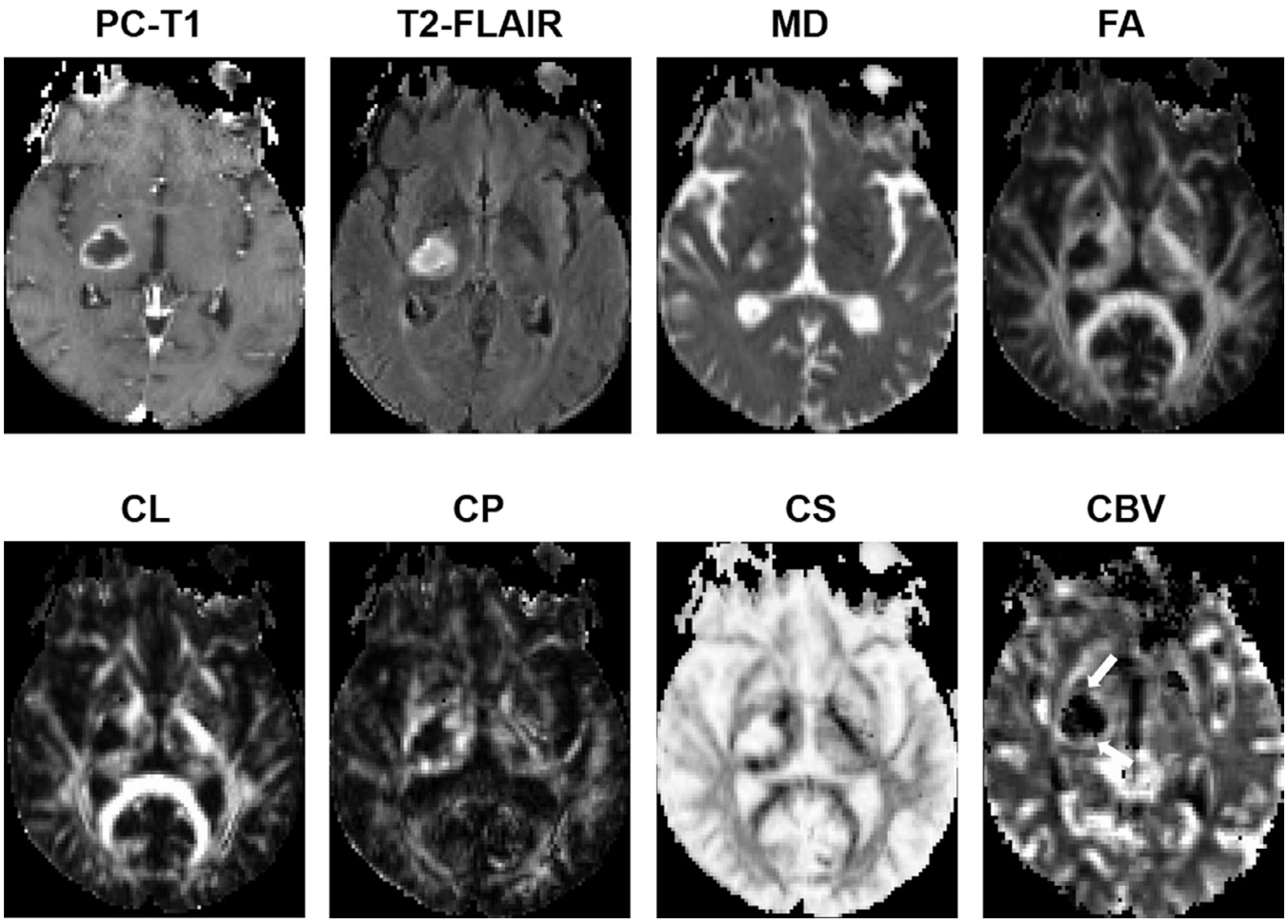


**FIGURE 11:**

Axial MR images from a 65-year-old patient with PsP. Postcontrast $T_1$-weighted image shows a heterogeneously enhancing lesion in the right thalamic region. Coregistered DTI-derived parametric maps and CBV maps are shown. CBV map shows moderately increased CBV from the lesion (white arrows). Decreased FA, CL, and CP and increased CS are observed from the enhancing part compared with normal white matter. Also, note the presence of lower CBV from contrast-enhancing regions compared to that from the TP patient shown in Fig. 10, suggesting a lower degree of perfusion and neovascularization in PsP compared to TP.

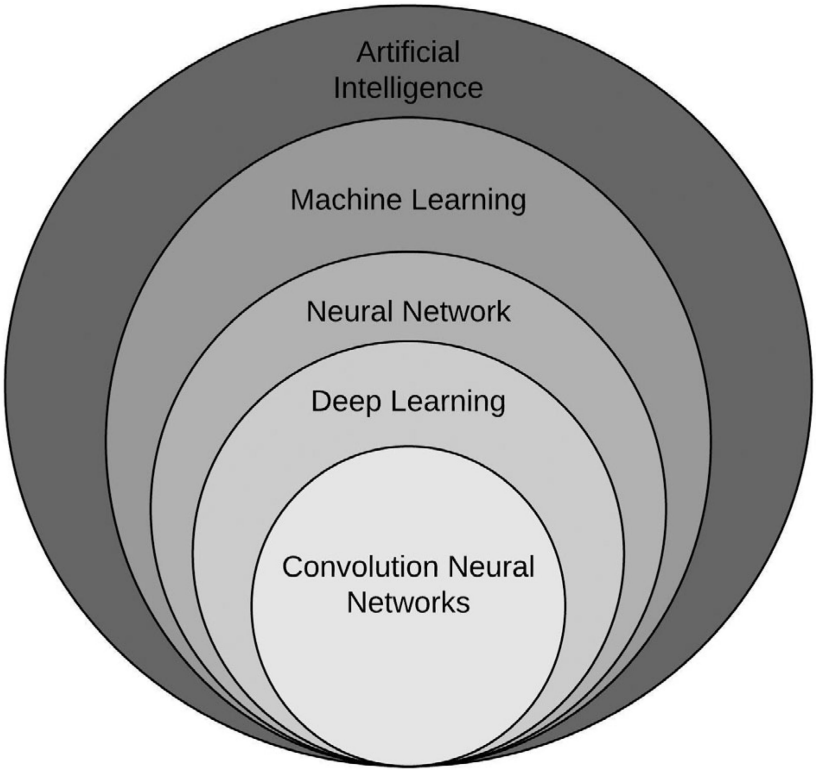


**FIGURE 12:**
Venn diagram demonstrating the hierarchy of artificial intelligence fields defined in the text.

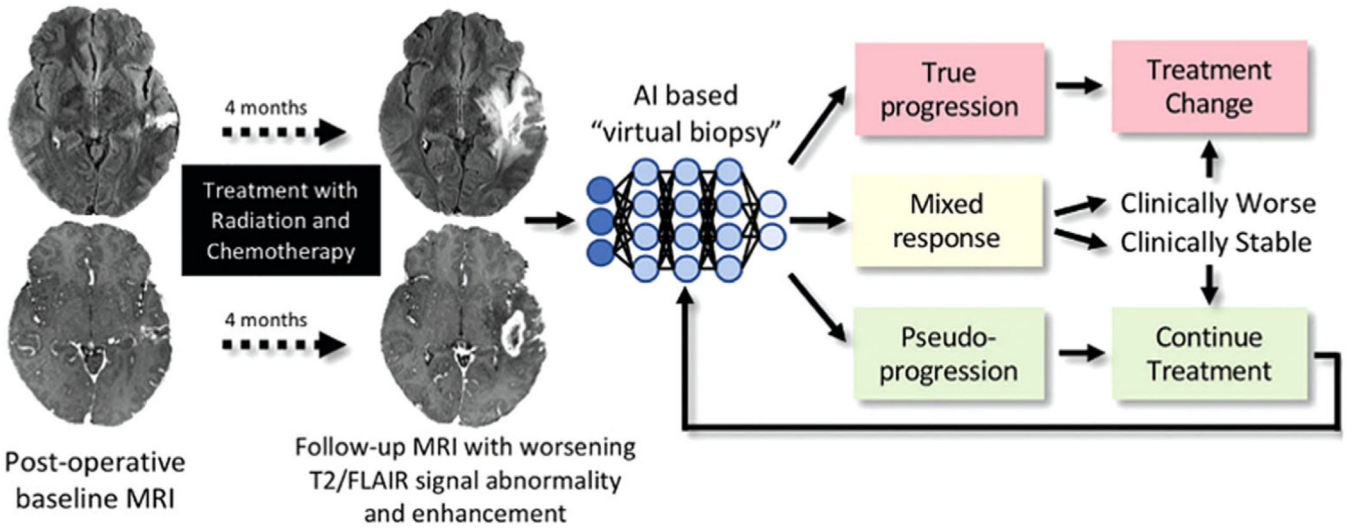


**FIGURE 13:**

Treatment response in neuro-oncologic imaging. After standard-of-care treatment with combined radiation therapy and chemotherapy, increasing $T_2$ FLAIR signal intensity abnormality and new and/or increasing size of enhancing lesions are often seen. AI-based "virtual biopsy" could assist in distinguishing underlying biology and segregating treatment response into three possible categories: true progression (>75% recurrent and/or residual glioma at pathologic examination), mixed response (25–75% recurrent and/or residual glioma at pathologic examination), and pseudoprogression (>75% treatment-related changes). Categories dictate distinct therapeutic approaches. In this example, the new enhancing lesion was found to represent 100% of treatment-related changes at pathologic examination, with few atypical cells. Reprinted with permission from Ref. 100 (Rudie et al., Radiology 2019 Mar; 290 (3):607–618).